



**HAL**  
open science

# Fluid Flow, Mineralization and Deformation in an Oceanic Detachment Fault: Microtextural, Geochemical and Isotopic Evidence From Pyrite at 13°30'N on the Mid-Atlantic Ridge

Andrew Martin, John Jamieson, Sven Petersen, Mostafa Fayek, Javier Escartin

## ► To cite this version:

Andrew Martin, John Jamieson, Sven Petersen, Mostafa Fayek, Javier Escartin. Fluid Flow, Mineralization and Deformation in an Oceanic Detachment Fault: Microtextural, Geochemical and Isotopic Evidence From Pyrite at 13°30'N on the Mid-Atlantic Ridge. *Geochemistry, Geophysics, Geosystems*, 2024, 25 (1), 10.1029/2023GC011033. insu-04734864

**HAL Id: insu-04734864**

**<https://insu.hal.science/insu-04734864v1>**

Submitted on 14 Oct 2024

**HAL** is a multi-disciplinary open access archive for the deposit and dissemination of scientific research documents, whether they are published or not. The documents may come from teaching and research institutions in France or abroad, or from public or private research centers.

L'archive ouverte pluridisciplinaire **HAL**, est destinée au dépôt et à la diffusion de documents scientifiques de niveau recherche, publiés ou non, émanant des établissements d'enseignement et de recherche français ou étrangers, des laboratoires publics ou privés.



Distributed under a Creative Commons Attribution 4.0 International License

# Geochemistry, Geophysics, Geosystems®



## RESEARCH ARTICLE

10.1029/2023GC011033

### Key Points:

- Microtextural, geochemical, and isotopic variations in subseafloor pyrite record the history of sample exhumation along a detachment fault
- Nickel and Co are remobilized and concentrated in pyrite across individual mineral grains in response to fluctuating fluid redox conditions
- Evidence of pyrite deformation and alteration mineralogy of samples indicates sample exhumation from a depth of 1–2 km

### Supporting Information:

Supporting Information may be found in the online version of this article.

### Correspondence to:

A. J. Martin,  
[Andrew.martin@unlv.edu](mailto:Andrew.martin@unlv.edu)

### Citation:

Martin, A. J., Jamieson, J. W., Petersen, S., Fayek, M., & Escartin, J. (2024). Fluid flow, mineralization and deformation in an oceanic detachment fault: Microtextural, geochemical and isotopic evidence from pyrite at 13°30'N on the Mid-Atlantic Ridge. *Geochemistry, Geophysics, Geosystems*, 25, e2023GC011033. <https://doi.org/10.1029/2023GC011033>

Received 3 MAY 2023

Accepted 4 NOV 2023

### Author Contributions:

**Conceptualization:** Andrew J. Martin  
**Data curation:** Sven Petersen  
**Formal analysis:** Andrew J. Martin, John W. Jamieson, Mostafa Fayek  
**Investigation:** Andrew J. Martin, John W. Jamieson  
**Methodology:** Andrew J. Martin, Sven Petersen

© 2024 The Authors. *Geochemistry, Geophysics, Geosystems* published by Wiley Periodicals LLC on behalf of American Geophysical Union. This is an open access article under the terms of the [Creative Commons Attribution License](https://creativecommons.org/licenses/by/4.0/), which permits use, distribution and reproduction in any medium, provided the original work is properly cited.

## Fluid Flow, Mineralization and Deformation in an Oceanic Detachment Fault: Microtextural, Geochemical and Isotopic Evidence From Pyrite at 13°30'N on the Mid-Atlantic Ridge

Andrew J. Martin<sup>1</sup> , John W. Jamieson<sup>2</sup> , Sven Petersen<sup>3</sup>, Mostafa Fayek<sup>4</sup>, and Javier Escartin<sup>5</sup> 

<sup>1</sup>Geoscience, University of Nevada, Las Vegas, NV, USA, <sup>2</sup>Department of Earth Sciences, Memorial University of Newfoundland, St. John's, NL, Canada, <sup>3</sup>GEO-MAR, Helmholtz Centre for Ocean Research Kiel, Kiel, Germany, <sup>4</sup>Department of Earth Sciences, University of Manitoba, Winnipeg, MB, Canada, <sup>5</sup>Laboratoire de Géologie (CNRS UMR8538), Ecole Normale Supérieure de Paris, PSL University, Paris, France

**Abstract** Hydrothermal fluids in ultramafic-hosted hydrothermal systems associated with oceanic detachment faults can be more oxidizing compared to mafic-hosted vent sites. These fluids form a mineral assemblage of pyrite, magnetite and hematite. At 13°30'N on the Mid-Atlantic Ridge, chlorite-quartz breccias recovered from an exposed fault scarp contain pyrite, with abundant magnetite and hematite, indicating that the redox of the fluids was variable. In primary micron-scale zonations in pyrite, Ni, Co, and Se have a decoupled relationship, recording fluctuations in the chemical composition and temperature of hydrothermal fluid as the grains grew. Secondary zonations that erase and overprint primary zonations are limited to the grain margin and permeable regions within the grain core. Secondary zonations formed via two processes: (a) grain dissolution followed by overgrowth, and (b) remobilization of metals during oxidizing fluid flow events. In both instances, Ni and Co have been mobilized and concentrated, and are not lost to the hydrothermal fluid. Superimposed on these features is evidence of grain scale deformation related to periods of fault movement along the detachment surface. Sulfur isotope ratios ( $\delta^{34}\text{S}$ ) in pyrite systematically decrease from the grain margin to the grain core, indicating that increased amounts of sulfur were derived from thermochemical sulfate reduction of seawater. Thus, pyrite records the evolution of fluid flow and deformation events during exhumation along the detachment surface from ~1 to 2 km below the seafloor at the base of the lava pile, with temporal fluctuations in fluid redox identified as an important process in controlling Ni and Co enrichment in pyrite.

**Plain Language Summary** Detachment faults are long lived faults that can expose ultramafic rocks at the seafloor. We aim to investigate the links between hydrothermal activity and detachment fault formation. To do this we use pyrite as a tape recorder for past fluid flow events. Across individual mineral grains, distinct zonations in metal content and sulfur isotope ratios show that the incursion of seawater occurred periodically during pyrite growth, increasing during fault movement events that lead to changes in the temperature and pH of the fluids in the fault zone. These changes concentrated metals toward the center of individual mineral grains. Zonations were then overprinted by later deformation-related events, providing evidence that the samples formed at deeper crustal levels below the seafloor and were progressively exhumed at the seafloor over time.

## 1. Introduction

Pyrite in seafloor massive sulfide (SMS) deposits and associated hydrothermal systems can act as a recorder for past hydrothermal fluid conditions, tracing temporal fluctuations in fluid pH, temperature, salinity and redox, that are preserved as micron-scale geochemical and isotopic variations across individual mineral grains (e.g., Martin et al., 2023). Assessing the relationship between faulting, fluid flow and mineralization is especially important in areas that have long, protracted growth histories characterized by multiple episodes of faulting, fluid flow and mineralization, such as oceanic core complexes and associated detachment fault zones (e.g., Escartin et al., 2017). We show that pyrite from a detachment fault zone records periods of more oxidizing fluid flow, which lead to distinct zonations in Ni and Co content and  $\delta^{34}\text{S}$  values across individual pyrite grains. These zonations in turn have been modified during deformation associated with continued slip events along the detachment fault surface. The response and behavior of metals to oxidizing fluid flow events can also be used more widely

**Resources:** Andrew J. Martin, John W. Jamieson, Sven Petersen, Mostafa Fayek, Javier Escartin

**Writing – original draft:** Andrew J. Martin

**Writing – review & editing:** Andrew J. Martin, John W. Jamieson, Sven Petersen, Mostafa Fayek, Javier Escartin

to understand the waning stages of hydrothermal activity where pyrite becomes oxidized to secondary minerals such as hematite, goethite and jarosite in SMS deposits (Herzig et al., 1991; Hu et al., 2022; Murton et al., 2019).

We investigated pyrite sampled at an exposed fault scarp at 13°30'N on the Mid-Atlantic Ridge (Escartin et al., 2017), where samples contained pyrite, magnetite and hematite, indicating that the redox state of the fluids was highly variable. The exposed fault scarp is interpreted to represent the detachment fault surface where lower crustal mafic material and serpentinite may be exhumed to shallow crustal depths or even the seafloor (Pierce et al., 2020). Samples with a similar mineral assemblage have only rarely been found on the modern seafloor, since the majority of the hydrothermal fluids are governed by the pyrite-pyrrhotite buffer at depth (Seyfried et al., 1999). Assemblages containing abundant magnetite, hematite and pyrite are documented from the Suye hydrothermal field on the Southwest-Indian Ridge (SWIR) (Liao et al., 2022), at Turtle Pits on the southern Mid-Atlantic Ridge (Haase et al., 2007), and in few samples from the ultramafic-hosted Logatchev field on the northern Mid-Atlantic Ridge (Dekov et al., 2018). They are also known to occur in several ancient volcanogenic massive sulfide (VMS) deposits (Almodóvar et al., 2019; Martin et al., 2018; Yıldırım et al., 2016). However, the origin of more oxidizing fluids, how these fluids evolve over time, and the effect these fluctuations have on trace metal enrichment processes remain poorly characterized. Using a combination of etching, geochemical mapping and systematic quantitative geochemical transects, we show that pyrite chemistry varies intricately at the micron scale. Primary micron scale zonations show evidence of post-formation deformation and are commonly overprinted by reaction fronts produced by oxidizing fluids, leading to the concentration of Ni and Co toward the grain core, providing linkages between deformation, fluid flow and faulting events in an oceanic detachment fault.

## 2. Geological Setting

The 13°30'N Oceanic Core complex (OCC) on the Mid-Atlantic Ridge (Figure 1a) is located on the western flank of the axial rift valley (Smith et al., 2008). The OCC detachment surface, delineated by well-developed surface striations is continuous in the direction of spreading for ~10 km and is approximately 4.5 km wide (Figures 1b and 1c) (Escartin et al., 2017; MacLeod et al., 2009; Pertsev et al., 2012). The OCC consists of serpentinitized peridotites, gabbros and occasional pillow basalt flows, and is considered to be inactive owing to the propagation of volcanic ridges to the north, and consequent termination of the detachment fault (Escartin et al., 2017; MacLeod et al., 2009). Five sites of sulfide accumulation and hydrothermal venting, four inactive and one active, occur at 13°30'N, collectively termed the Semenov vent field cluster (Cherkashev et al., 2013; Melekestseva et al., 2014; Pertsev et al., 2012). Only Semenov-2 remains hydrothermally active, whilst Semenov-1, -3, -4, and -5 are inactive (Figure 1b).

## 3. Methods and Sample Collection

### 3.1. Sample Collection

The magnetite-pyrite-rich samples analyzed in this study (Cruise samples V558-347 and V558-357, and corresponding IGSN number CNRS0000000351 and CNRS0000000361) were collected during the 2013 ODEMAR cruise aboard the *N/O Pourquoi Pas?* (IFREMER, France) (<https://doi.org/10.17600/13030070>). Sample collection was conducted using the ROV Victor6000 (IFREMER, France; Escartin, 2014). The two samples in this study were collected 90 m apart at water depths of 2,801 m and 2,820 m along a sub-vertical cliff in the Semenov-4 area (Table 1; Figures 2a). This cliff corresponds to a fault scarp facing WSW that dissects the detachment near its termination. This scarp provides a cross-sectional exposure through the footwall, and of the now inactive detachment fault (Figures 1c and 2a). A video of the sample collection can be found here: <https://video.ifremer.fr/video?id=13466>.

Seafloor observations suggest two possible scenarios explaining the origin of the samples analyzed here: (a) samples are from the detachment fault zone and therefore record fluid flow-deformation interaction that occurred at depth, while the detachment fault was still active or (b) the origin of sulfide mineralization is related to the nearby Semenov-4 hydrothermal field and occurred in response to later faulting that cross-cuts the toe of the detachment forming a graben structure.

### 3.2. Analytical Methods

#### 3.2.1. Whole-Rock Geochemistry

The hydrothermal samples ( $n = 3$ ) were crushed, powdered in an agate mill (Pulverisette 5 by Frisch), and analyzed commercially at ACTLABS (Ancaster, Canada) for their major and trace element composition using

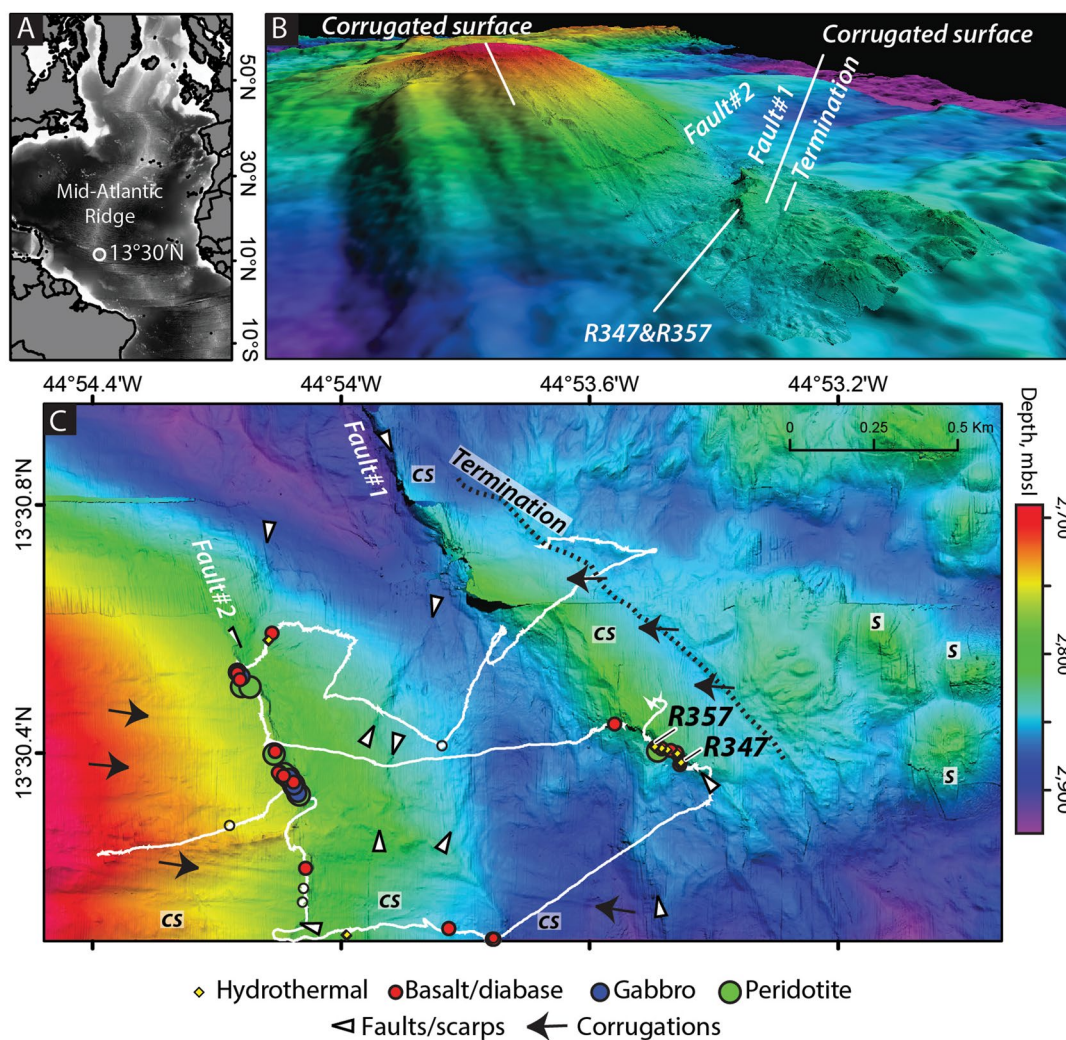


**Figure 1.** Location map of 13°30'N on the Mid-Atlantic Ridge. (a) Location of Semenov on the Mid-Atlantic Ridge. (b) 3D view looking NW toward the oceanic core complex (depth key as for image C). (c) Detailed map of the Semenov-4 area showing the location of the ROV dive (white line), fault structures (white arrows), corrugations (black arrows), dominant lithology sampled and the location of samples analyzed in this study (R357 and R347), located proximal to the detachment termination. Bathymetry data from Escartin et al. (2017), and available from Escartin and Petersen (2017). CS = corrugated surface, S = sulfide material.

a combination of methods, including inductively coupled plasma-atomic emission spectroscopy, inductively coupled plasma-mass spectrometry, and instrumental neutron activation (Table S1 in Supporting Information S2). High-purity burnt and acid-treated quartz-sand, iso-2-propanol, and deionized water were used for cleaning in between samples. In order to control the accuracy of the measurements, two certified international reference materials (standards CCu-1c and CZn-3; Table S1 in Supporting Information S2) were prepared and analyzed as unknown samples along with the other samples.

### 3.2.2. Mineralogy and Etching

Representative samples were prepared as both polished mounts and thin sections ( $n = 6$ ), from the hand specimen sample shown in Figure 2b. Transmitted light microscopy was undertaken on thin section samples to identify alteration minerals present. Reflected light microscopy and etching were undertaken on the remaining four polished mounts. Quantitative mineralogy, to determine modal mineral abundance, was undertaken using an FEI Quanta 400 Scanning Electron Microscope at Memorial University of Newfoundland (Canada), employing an operating voltage of 25 kV with a 2  $\mu\text{m}$  pixel size and a step size for x-ray acquisition of 4 pixels.

Etching was performed using sodium hypochlorite (NaOCl) for 90 s, then samples were rinsed with water and air dried. This method tarnishes the pyrite surface and can be used to delineate internal zonations and sub-grain

**Table 1**  
*Chemical Composition and Sample Description/Location Information of Pyrite-Magnetite-Hematite-Bearing Samples From the Semenov-4 Hydrothermal Field, Mid-Atlantic Ridge*

Sample Location	V558-347 13°30.392'N/44°53.457'W 2820m	V558-357A 13°30.420'N/44°53.501'W 2801m	V558-357C 13°30.420'N/44°53.501'W 2801m
Depth			
IGSN No.	CNRS0000000351		CNRS0000000361
wt. %			
Cu	<0.01	0.01	0.15
Zn	<0.01	<0.01	<0.01
Fe	46.8	39.8	37.5
S	23.1	28.6	23.2
SiO <sub>2</sub>	5.78	20.8	16.0
MgO	3.61	0.75	6.17
Al <sub>2</sub> O <sub>3</sub>	0.83	0.76	5.27
TiO <sub>2</sub>	<0.01	0.05	0.18
ppm			
Au	<0.01	0.02	<0.01
Ag	<3	<3	<3
As	33	34	15
Ba	7	13	<3
Bi	<2	<2	<2
Cd	<2	<2	<2
Co	387	443	96
Cr	1,580	2,150	2,300
Hg	<0.005	<0.005	<0.005
In	<0.2	<0.2	<0.2
Mn	62	44	145
Mo	8	37	10
Ni	860	990	1,580
Pb	<0.8	5.3	<0.8
Sb	0.3	0.3	0.6
Sc	3.7	3.2	14.3
Se	45	32	41
Sn	14.4	1.2	4.3
Te	<6	<6	<6
Tl	<0.2	<0.2	<0.2
U	0.5	0.6	0.3
V	116	183	153
Y	2.7	4.9	4.7

Note. Analyses with < are below the detectable limit.

mineral boundaries. The tarnish was easily removed using a polishing pad and a diamond suspension polishing solution.

### 3.2.3. Qualitative Geochemical Mapping of Pyrite

Geochemical maps of representative pyrite grains were undertaken using an Electron Probe Micro-Analyzer (EPMA). All maps were acquired using an accelerating voltage of 20 kV, a beam current between 250 and

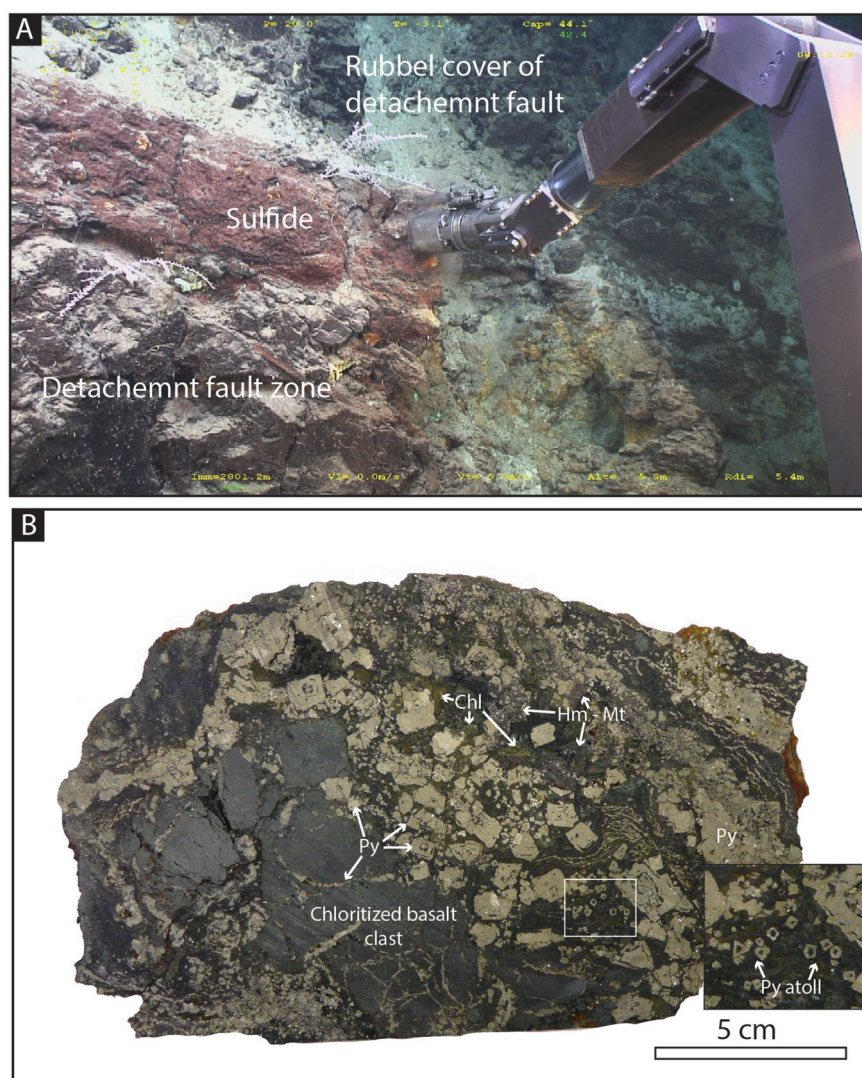


**Figure 2.** (a) Image showing sample collection at the seafloor (V558-357). An exposed sulfide vein occurs on a face interpreted as a fault scarp. (b) Photo of the cut sample surface analyzed in this study. Host rock clasts are cross-cut by a network of pyrite veins. The matrix contains coarse-grained euhedral pyrite, commonly with atoll structures (inset image) in a cement of hematite, magnetite, chlorite and quartz. Py = pyrite, Hm-Mt = hematite-magnetite, Chl = chlorite.

300 nA, a dwell time of 50–200 ms and a step size of 1–3  $\mu\text{m}$ , depending on the size of the grain analyzed. Maps were collected using two EPMA instruments: a JEOL JXA-8530F+ at the University of Minnesota (U.S.) and a JEOL JXA-8230 at the Memorial University of Newfoundland (Canada). Each instrument was equipped with up to five wavelength dispersive spectrometers allowing the simultaneous detection of Co, Ni, Se, and Cu. Element concentrations were not quantified during mapping, hence only relative changes in metal content can be assessed.

### 3.2.4. Quantitative Geochemistry of Pyrite

The trace metal content of pyrite ( $n = 168$  spots, 2 lines) was determined using laser ablation inductively coupled plasma mass spectrometry (LA-ICP-MS) on four representative polished mounts. LA-ICP-MS analysis was performed at Memorial University of Newfoundland (Canada) using a GeoLas 193 nm laser coupled to a Thermo-Finnigan Element XR ICP-MS. Analysis employed a spot diameter of 40  $\mu\text{m}$  at a frequency of 5 Hz and a fluence of 3 J/cm<sup>2</sup>. Each analysis lasted 50 s and a gas blank was measured for 30 s prior to each analysis. Lines were conducted under the same analytical parameters as spot analyses and the sample translated relative to the laser at 15  $\mu\text{m/s}$ . Analyte masses measured included <sup>51</sup>V, <sup>53</sup>Cr, <sup>55</sup>Mn, <sup>59</sup>Co, <sup>60</sup>Ni, <sup>65</sup>Cu, <sup>66</sup>Zn, <sup>69</sup>Ga, <sup>72</sup>Ge, <sup>75</sup>As

,  $^{77}\text{Se}$ ,  $^{95}\text{Mo}$ ,  $^{109}\text{Ag}$ ,  $^{111}\text{Cd}$ ,  $^{115}\text{In}$ ,  $^{118}\text{Sn}$ ,  $^{121}\text{Sb}$ ,  $^{125}\text{Te}$ ,  $^{197}\text{Au}$ ,  $^{205}\text{Tl}$ ,  $^{206}\text{Pb}$ , and  $^{209}\text{Bi}$ . Iron-57 was used as an internal standard for all analyses and stoichiometric Fe content of 46.5% was assumed for pyrite. External calibration was performed using USGS MASS-1 and NIST 610. Precision was monitored through the repeat analysis of MASS-1 ( $n = 26$ ) that yielded a relative standard deviation (RSD) for Bi, Pb, As, Zn, Cu, and Mn of <10%, and <13% for V, Cr, Ni, Ga, Ge, Mo, Ag, Cd, In, Sn, Sb, and Au. Only Te, Se, and Co showed a higher RSD, reaching 18%, 13% and 18%, respectively (see Table S2 in Supporting Information S2). Subtraction of gas blanks and calculation of detection limits were performed using Iolite software.

### 3.2.5. Sulfur Isotope Analysis

The sulfur isotopic composition ( $\delta^{34}\text{S}$ ) of pyrite ( $n = 45$ ) was obtained using secondary ion mass spectrometry (SIMS) microanalysis in three polished mounts. Samples were mounted in epoxy resin with aluminum retaining rings, polished, and then coated with 300 Å of Au to mitigate the charging of the sample during ion bombardment. Analyses were performed using a Cameca IMS 7f SIMS instrument equipped with a ETP 133H electron multiplier at the University of Manitoba (Canada). Each sample was bombarded with a primary ion beam of 3 nA of Cs<sup>+</sup> accelerated through a potential voltage of 10 KeV and focused into a 10 μm spot. Negatively charged secondary ions were accelerated into the mass spectrometer using a potential of +8.7 KeV. Each spot was pre-sputtered for 120–180 s prior to analysis to exclude sulfur contamination from the sample surface. Each analysis lasted 7 min and included 50 cycles (1 s of detection on 32 and 5 s on 34S). The reproducibility of results was calculated based on the repeat analysis of standard reference material Balmat Pyrite (15.1‰) (Crowe & Vaughan, 1996), and to correct for instrumental mass fractionation. The spot-to-spot reproducibility was better than ±0.3‰ (Table S3 in Supporting Information S2). All analyses are reported in standard delta notation ( $\delta^{34}\text{S}$ , ‰) relative to Vienna-Canyon Diablo Troilite (V-CDT).

## 4. Results

### 4.1. Sample Characterization

In hand specimen, dark sub-angular clasts of chloritized basalt are cross-cut by a network of pyrite-bearing stringers (Figure 2b). Aggregates of coarse-grained (up to ~1 cm) euhedral pyrite surround rock clasts, occurring in a matrix of quartz, magnetite, hematite, chrome spinel, and chlorite. Many pyrite grains exhibit skeletal or atoll-like textures (Figure 2b—inset). Mineral relationships in two representative samples are shown in Figures 3 and 4. One section contains notably more magnetite and hematite (classified as iron oxide in Figure 3b) whereas the other section is more chlorite-rich (Figure 4). In both samples, pyrite is spatially associated with magnetite, hematite, and quartz (Figures 3, 4c, and 4d), with minor amounts of rutile (Figures 4e and 4f) and apatite (Figure 4b; <<1 modal %). It should be noted that magnetite and hematite are not exclusively associated with pyrite and have a wide spatial distribution in the samples (Figures 3b and 4b). Chrome spinel occurs associated with both chlorite, quartz-pyrite-rich veins and disseminated in the magnetite-rich matrix (Figures 3b and 4b). In one sample analyzed chalcopyrite occurs as a discrete grain associated with quartz and lesser amounts of iron-oxide in a vein (Figures 4a and 4b).

Pyrite generally retains its euhedral morphology (Figure 5a), but is variably resorbed in its core (Figures 5b–5e) or more rarely outer margins (Figures 5e and 5f). Pyrite is overgrown by magnetite and hematite, most prolifically toward the margin of the grains (Figures 5d–5f), with some grains appearing more affected than others (e.g., Figure 5a vs. Figure 5f). Hematite occurs as singular radiating euhedral crystal clusters within pyrite (Figures 5a, 5d, and 5f) and in the matrix associated with quartz and magnetite (Figures 5g and 5h). Magnetite occurs as elongate laths (Figures 5d, 5g, and 5h), as euhedral grains (Figures 5a and 5d) and as coarse subhedral grains (Figures 5b and 5i). Chrome spinel occurs as anhedral grains that have a lighter, often highly pitted alteration rim (Figure 5j). Mineral maps indicate that the rim is Fe-rich, most likely magnetite (Figures 3 and 4b). Chalcopyrite is associated with pyrite and quartz in veins or in clasts in the chloritized matrix (Figures 5l and 5k).

### 4.2. Microtextural Analysis

Etching of pyrite grains reveals complex internal zonations (Figure 6). Bright zones delineate concentric zonations that are both parallel and sub-parallel to the current grain margin (Figure 6a). The zones that appear the brightest in color, and delineate a relict core zone are generally free from hematite and magnetite inclusions (Figures 6a and 6b). In some subhedral pyrite grains, internal zonations appear as intricate irregular bands that

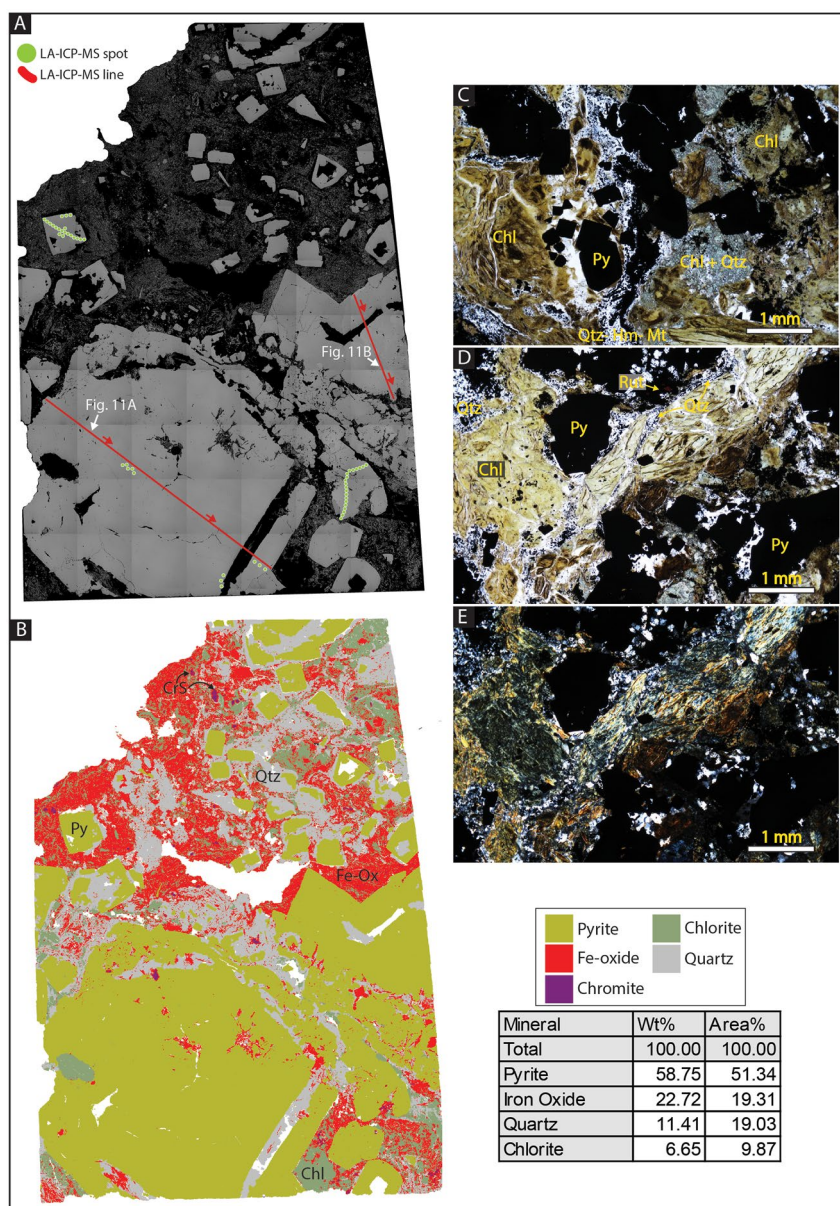


**Figure 3.** Sample characterization. (a) Back scattered electron (BSE) image of V558-357 showing the location of LA-ICP-MS spot and line analyses (green and red lines). Note that vertical and horizontal lines showing a change in contrast are an analytical artifact. (b) Mineral map of sample corresponding to mineral abundances shown in the inset table. Pyrite is spatially associated with networks of quartz, hematite-magnetite (Fe-oxide) and chlorite-rich veins. Chrome spinel grains are spatially associated with pyrite and matrix material. (c) Image in plane polarized light (PPL). The matrix is composed of abundant chlorite from relict wall rock clasts with quartz containing hematite, magnetite and pyrite. (d) Image in PPL. Network of quartz, hematite, and pyrite veins crosscutting chlorite-rich material. Rutile occurs as an accessory phase at the margin of quartz veins. (e) Image in cross-polarized light (XPL), same as in image (d). Qtz = quartz, Chl = chlorite, Py = pyrite, Mt = magnetite, Hm = hematite, Rut = rutile, CrS = chrome spinel.

are randomly oriented (Figures 6c and 6d). Two distinct generations of zonation are evident in some pyrite grains (Figures 6e–6i). Intricate parallel zonations are truncated and erased near the margins of the grains (Figures 6e–6i). A bright zone, located several microns from the grain margin, forming a rind, is observed at the truncation between the different zonations (Figures 6e–6i). Individual concentric zonations, delineated by alternating dark and light bands occur at the scale of 2–3  $\mu\text{m}$  (or less) (Figure 6h), and in some samples show unusual features where bands have a kinked appearance and coalesce into more massive homogenous areas, termed “streaky fabric” (Figure 6h). As the margin of the grain is approached, the zonations are destroyed

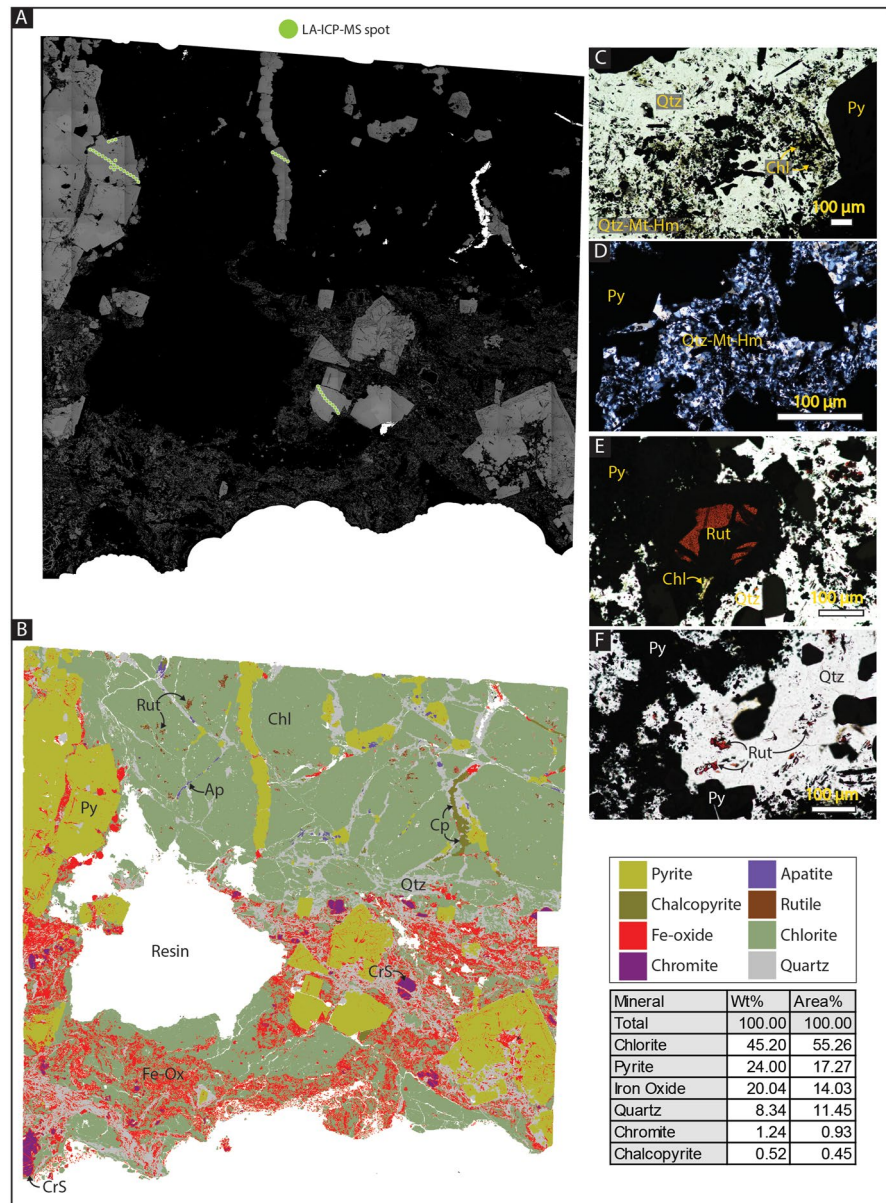


**Figure 4.** Sample characterization (a) Back scattered electron (BSE) image of V558-357. Note that vertical and horizontal lines showing a change in contrast are an analytical artifact. The locations of LA-ICP-MS analyses are shown in green. The sample is silica/chlorite-rich compared with Figure 3. (b) Mineral map of sample corresponding to mineral abundances shown in the inset table. Chlorite-rich wall rock clasts are cross-cut by networks of pyrite (and chalcopyrite)-rich veins that are associated with quartz-rutile-apatite veins. Coarse-grained chrome spinel occurs throughout the sample. Hematite and magnetite (Fe-oxide) occur spatially associated with quartz. (c) Image in PPL showing quartz-hematite-magnetite vein with minor chlorite and pyrite. (d) Image in XPL, same as in image (c). (e) Image in PPL showing a large rutile grain associated with a quartz vein. The vein contains minor chlorite. (f) Image in PPL showing fine-grained rutile intergrown with quartz. Py = pyrite, Mt = magnetite, Hm = hematite, Chl = chlorite, Qtz = quartz, Rut = rutile, CrS = chrome spinel.

(Figure 6i). Similar micron-scale zonations were a common feature in many of the pyrite grains analyzed (Figures 6j and 6k). In one sample, zonations are cross-cut and destroyed by a ~150 μm wide “channel structure” (Figure 6l) that occurs perpendicular to the direction of zonations and is spatially associated with magnetite grains.

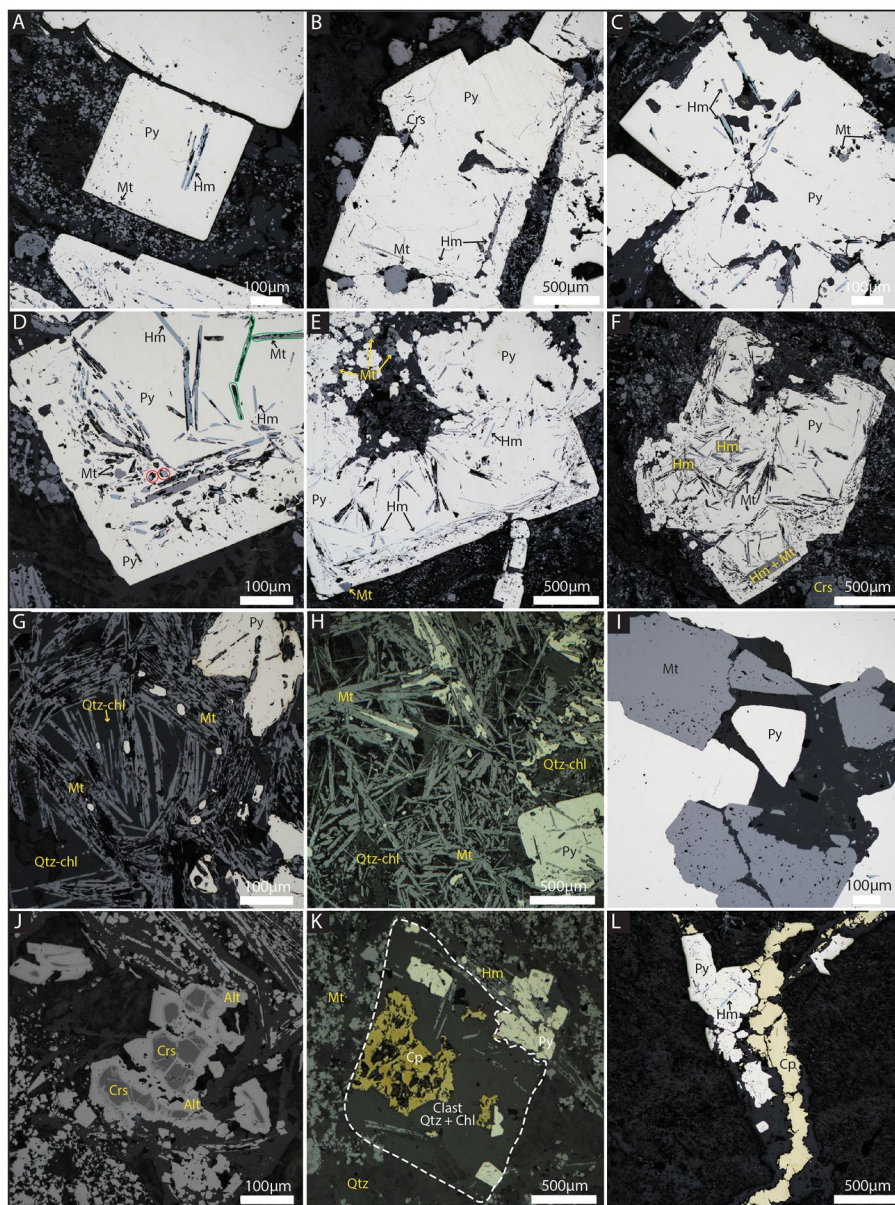


**Figure 5.** Photomicrographs in reflected light from sample V558-357 (a–g, i, j, and l) and –347 (h and k). (a) Euhedral pyrite with a euhedral hematite grain in the core and fine-grained magnetite. (b) Inclusions of hematite, coarse-grained magnetite and chrome spinel in euhedral pyrite. (c) Subhedral pyrite with high porosity zones containing hematite and magnetite infilling porosity. (d) A euhedral pyrite that has been extensively overgrown at its margin by pyrite, magnetite and hematite. Hematite pseudomorphs magnetite in some grains (red circles) or vice versa (green lines). (e) Pyrite grain with a resorbed core replaced with magnetite, hematite and quartz. The grain rim also contains a zone of magnetite-hematite-rich pyrite. (f) A cluster of pyrite veins that have been resorbed with a subhedral morphology that has been extensively overgrown by magnetite and hematite. (g) Matrix of euhedral hematite with disseminated anhedra pyrite in a quartz-chlorite matrix. (h) Matrix of magnetite laths intergrows with quartz and chlorite with pyrite. (i) Coarse-grained magnetite with a pitted resorbed appearance associated with pyrite. (j) Near complete alteration of chrome spinel grains to Fe-oxide. (k) A mafic chlorite-rich clast containing chalcopyrite surrounded by quartz and overgrown by pyrite at its margins. (l) Chalcopyrite vein with pyrite and hematite. Py = pyrite, Hm = hematite, Mt = magnetite, Qtz = quartz, Chl = chlorite, Crs = chrome spinel, Alt = Fe-alteration.

### 4.3. Geochemical Mapping

In all samples we analyzed, the bright bands identified during etching were due to enrichment in Ni or Co or both Ni + Co (Figures 7–9). The distribution of Cu in the two euhedral pyrite grains analyzed was homogeneous

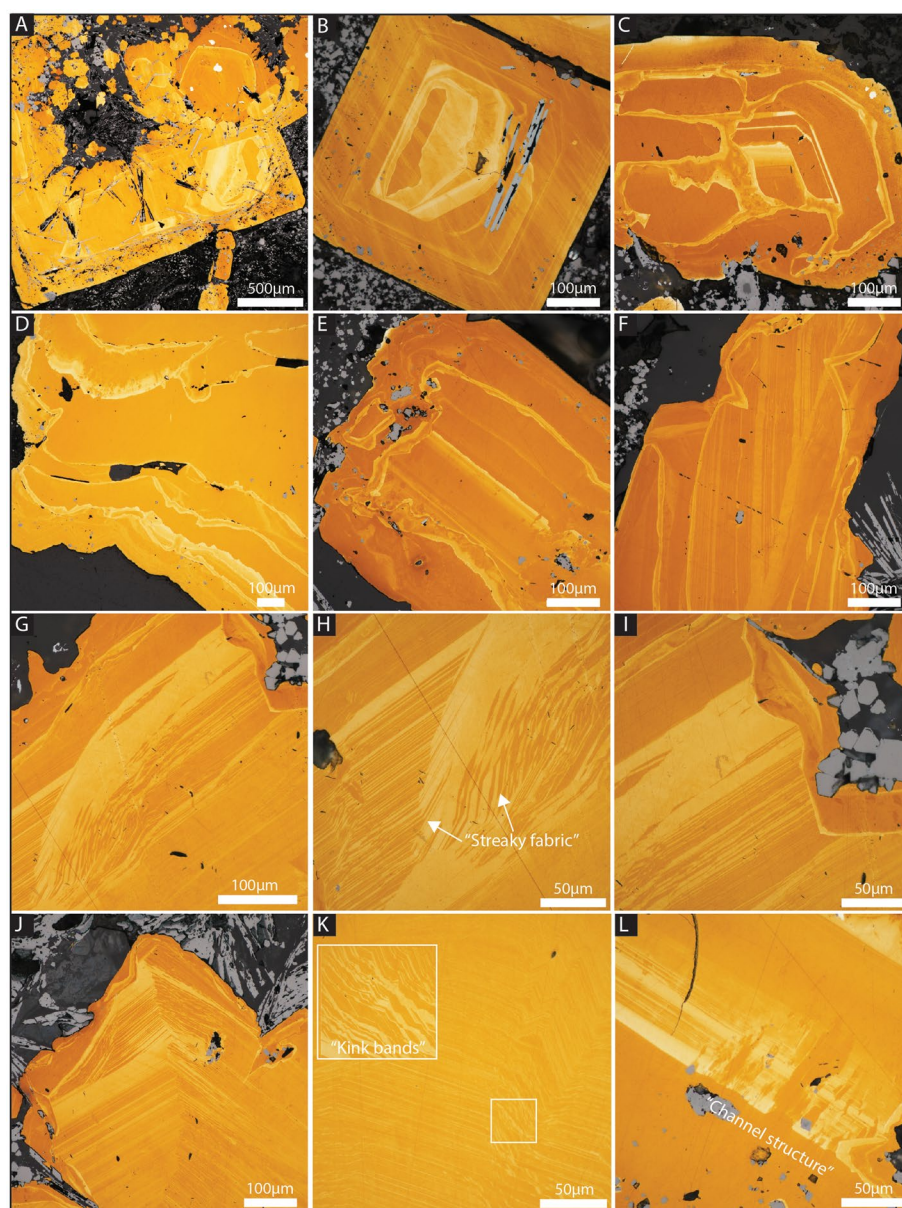


**Figure 6.** Photomicrographs in reflected light of etched samples. (a) Pyrite grain with a highly resorbed core and a rim overgrown by hematite and magnetite (see Figure 5E). Bright relict cores that are inclusion-poor are visible. (b) Pyrite with a bright core and concentric zonations with hematite and magnetite (see Figure 5A). (c) Subhedral pyrite with frilly irregular zonations. (d) Irregular zonations in pyrite with bright zones following inclusion or vug-rich areas. (e) Concentric zonations in pyrite overprinted by frilly zonations. (f) Pyrite with concentric zonations that are overprinted at the grain margin. (g) Streaky fabric in pyrite where micron-scale bright zonations coalesce. Note also that overprinting occurs at the grain margin. (h) Zoomed in the image of the streaky fabric. (i) Overprinting of micron-scale zonations at the grain margin. (j) Concentric zonations in pyrite—note overprinting at the grain margin and surrounding magnetite. (k) Micron-scale zonations with a stepped offset appearance, termed here as “kink bands.” (l) Concentric zonations that have been destroyed by a “channel structure” in the vicinity of magnetite grains.

(Figures 7c and 7i). The cobalt distribution is more complex, with enriched rims mantling zones of high Ni content, which is especially prevalent in the core of the grain (Figures 7d and 7j). Nickel is highly concentrated in the grain core with a strong correlation between the brightest bands identified during etching and Ni enriched zones (Figure 7 B and H). Selenium shows no detectable variation from the core to the rim of the grains analyzed (Figures 7c and 7l). Magnetite and hematite do not preferentially host Ni, Co, Se, or Cu in the grains analyzed (Figure 7).

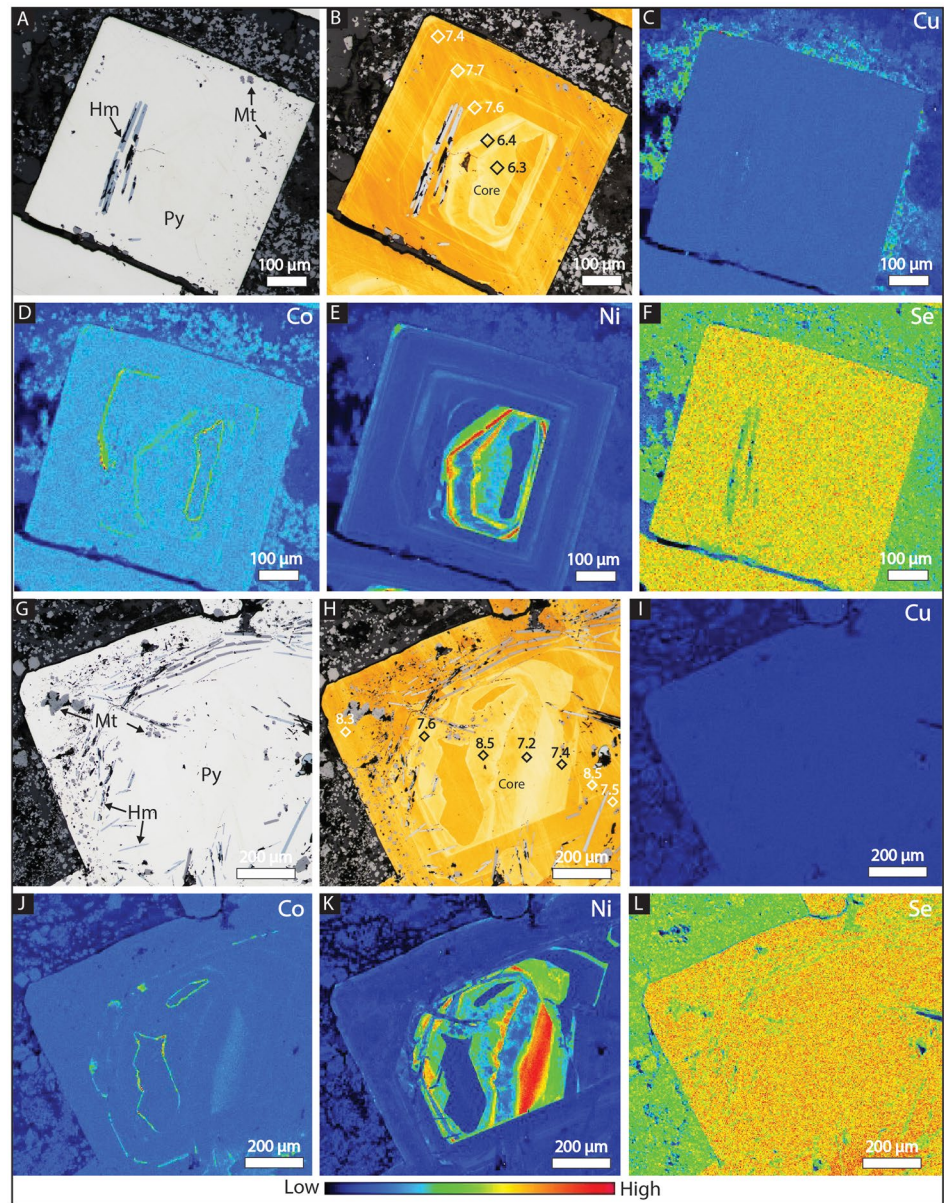


**Figure 7.** Element distribution maps of pyrite. (a) Reflected light image. (b) Etched image with the location of SIMS sulfur isotope analytical points. A bright core zone can be delineated. (c) Cu, (d) Co, (e) Ni, (f) Se. The core is strongly enriched in Ni with a rind of Co enrichment. Copper and Se are homogeneously distributed. (g) Reflected light image. (h) Etched image with the location of SIMS sulfur isotope analytical points. (i) Cu, (j) Co, (k) Ni, (l) Se. The core is strongly enriched in Ni, mantled by a zone of Co enrichment. Note that magnetite and hematite do not contain high Ni or Co. Se and Cu are homogeneously distributed.

In samples where random zonation occurs (Figure 8a), the brightest areas in the etched image (Figure 8b) correlate with the Ni and Co distribution. Copper does not show any discernible zonation (Figure 8c). Cobalt is enriched only in the core of the grain and in two pronounced concentric zonations that are parallel to the core (Figure 8d). The cobalt distribution weakly correlates with Ni, with Co enrichment mantling zones of high Ni content (Figure 8d vs. Figure 8e). Nickel occurs in zonations that are broadly parallel to the current grain margin or areas that are inclusion-rich (Figure 8e). Selenium distribution does not correlate with either Ni or Co, instead it is enriched in areas that appear darker in color that are surrounded by Ni and Co enriched zones (Figure 8f).

In samples where intricate zonations are overprinted at the grain margin (Figure 8g), clear trends in metal distribution exist (Figure 8h). As observed in previous examples, the bright zones identified in the etched image

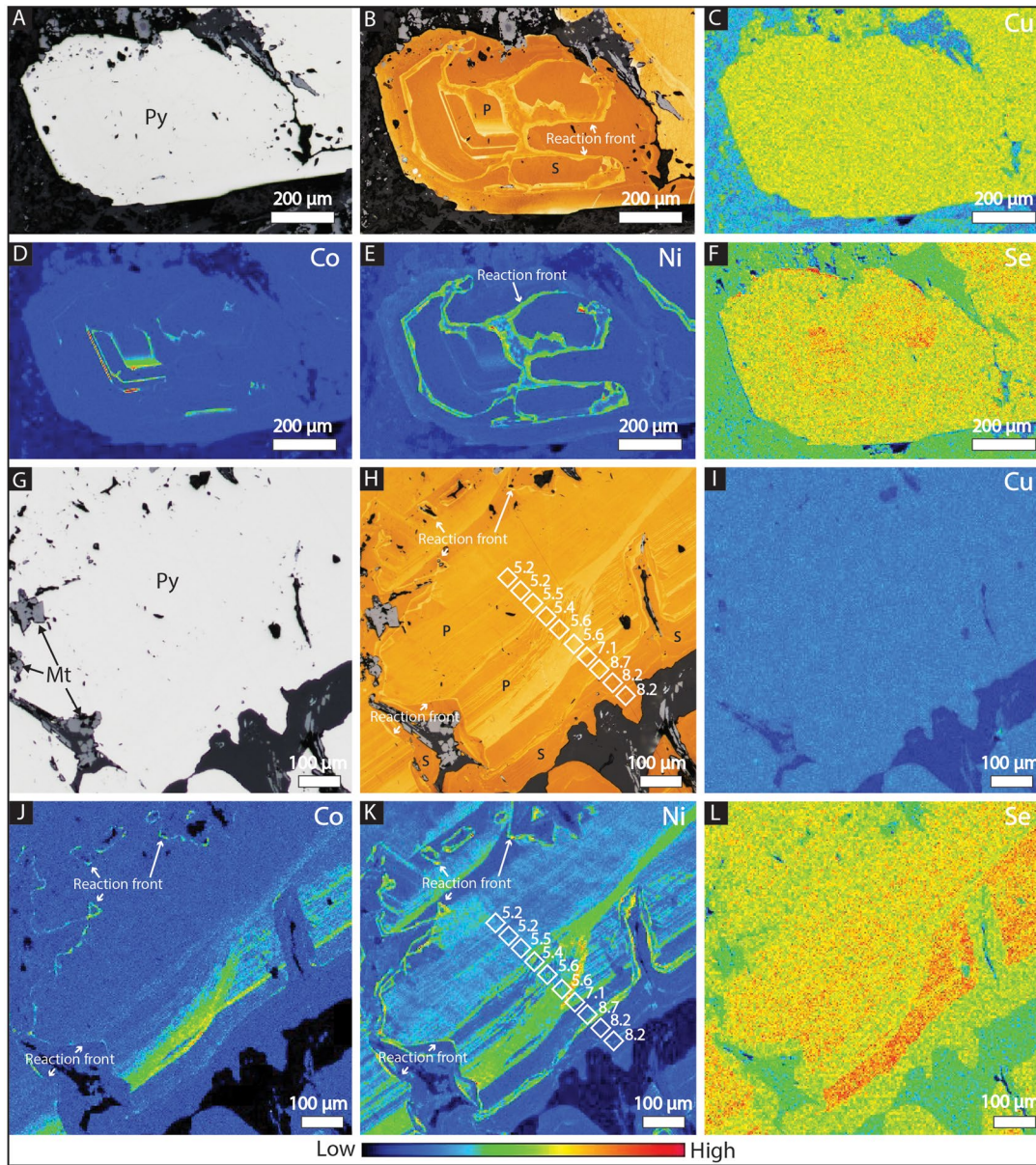


**Figure 8.** Element distribution maps of pyrite. (a) Reflected light image. (b) Etched image with the location of SIMS sulfur isotope analytical points. (c) Cu, (d) Co, (e) Ni, (f) Se. The core zone is strongly enriched in Co-forming concentric zonations. The core is also slightly enriched in Se. Nickel is enriched in a series of frilly zonations that cause subparallel to the grain margin. Copper is homogeneously distributed. (g) Reflected light image. (h) Etched image with the location of SIMS sulfur isotope analytical points. (i) Cu, (j) Co, (k) Ni, (l) Se. Bright bands in the etched image are Ni and Co enriched. Selenium shows the inverse relationship to Ni and Co. The margin of the grain is relatively depleted in Ni, Co and Se. Copper is homogeneously distributed. P = primary, S = secondary.

correspond to Ni and Co distribution. Copper is homogeneously distributed (Figure 8i). Cobalt is enriched in a narrow rind that runs parallel to the present-day grain margin and is depleted toward the margin of the grain (Figure 8j). Cobalt is also strongly enriched in the micron-scale concentric zonations, especially where the zonations coalesce (Figure 8j). As observed with Co, Ni is also concentrated in the rind and depleted around the margin of the grain (Figure 8k). The rind is continuous, and in some areas, an outer and inner rind can be delineated, one that occurs before the area of Co enrichment (Figure 8k). Nickel is also enriched in micron-scale concentric zonations (Figure 8k). Selenium shows the inverse relationship to Ni and Co and is relatively enriched in Ni and Co-poor zones (Figure 8l). Selenium does not form a rind around the margin of the grain, but micron-scale zonations are truncated near the grain margin at the same point as Ni and Co (Figure 8l vs. Figure 8k).

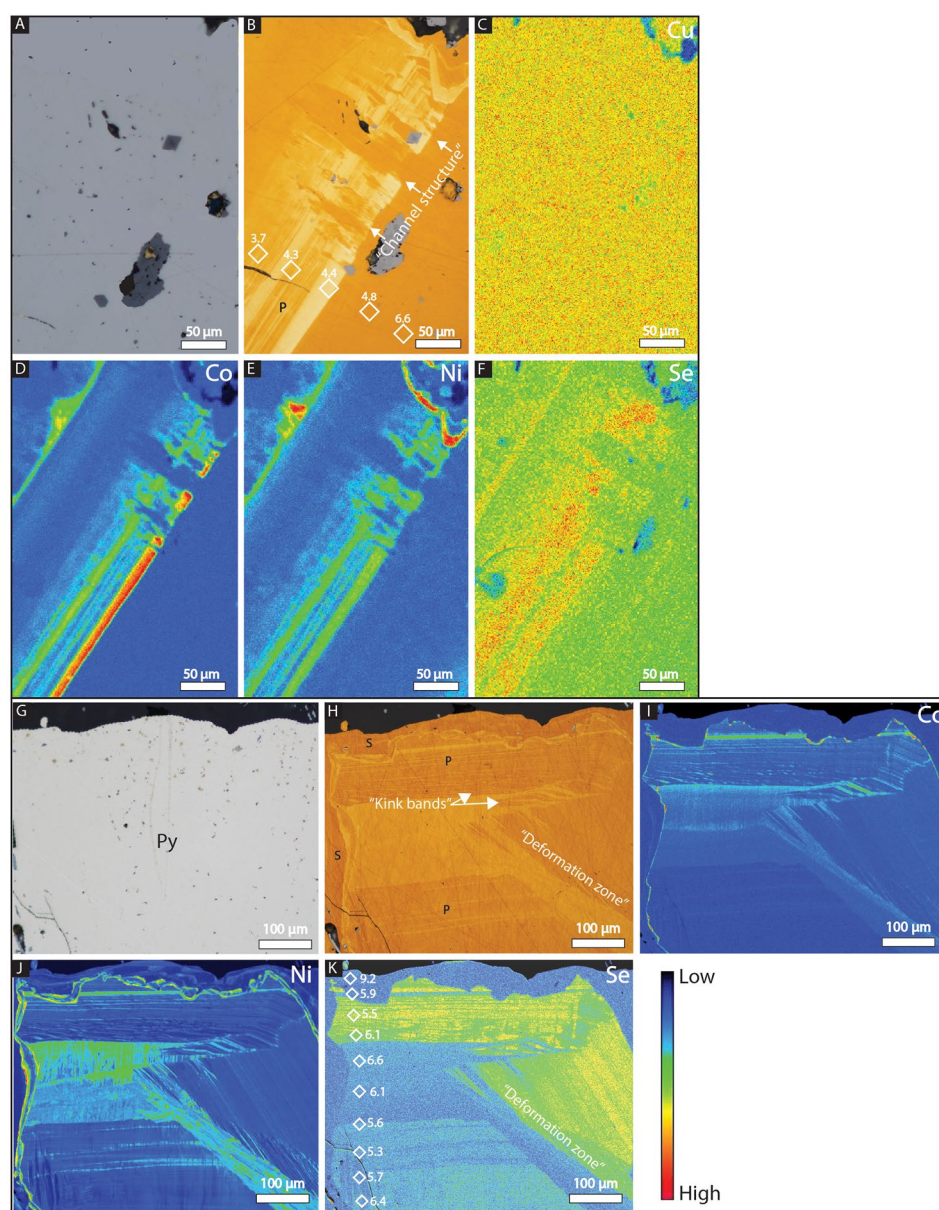


**Figure 9.** Element distribution maps of pyrite. (a) Reflected light image. (b) Etched image with the location of SIMS sulfur isotope analytical points. (c) Cu, (d) Co, (e) Ni, (f) Se. Concentric zonations that are enriched in Co, Ni and Se, showing the inverse spatial distribution are cross-cut and destroyed by a “channel structure.” Copper is homogeneously distributed. (g) Reflected light image. (h) Etched image with the location of SIMS sulfur isotope analytical points. (i) Co, (j) Ni, (k) Se. Concentric zonations that are enriched in Ni, Co and Se, with Se showing the inverse distribution to Ni and Co. At the grain margin, zonations are overprinted. Superimposed on these features are “kink bands” and a “deformation zone.” P = primary, S = secondary.

The “channel structure” identified by an area where concentric zonations are destroyed, and cross-cut (Figures 9a and 9b) is clearly identified in the Co, Ni, and Se distribution maps (Figures 9d–9f). The “channel” is relatively depleted in Co, Ni and Se compared with surrounding pyrite. Copper is homogeneously distributed (Figure 9c). Cobalt is strongly enriched in concentric zonations that occur as bright bands in the etched image (Figure 9d). Nickel distribution correlates with Co distribution in the concentric zonations (Figure 9e). At the edge of the grain, concentric zonations are overprinted and Ni is strongly enriched (Figure 9e). Selenium shows the inverse relationship to Ni and Co (Figure 9f); it is enriched between the Ni and Co-rich zones.

High-resolution (1  $\mu\text{m}$  step size) mapping was undertaken on one sample to investigate the relationship between Ni, Co and Se (Figures 9g–9k). A pronounced rim that is strongly depleted in Co that truncates and erases micron-scale concentric zonations occurs (Figure 9i). Nickel enrichment shows the same distribution as Co, with the notable exception that the rind for Ni is wider and appears to have two distinct enrichment zones compared with one for Co (Figure 9i vs. Figure 9j). Selenium distribution negatively correlates with Co and Ni distribution, with concentric zonations discernible on the micron-scale (Figure 9i). Selenium is depleted at the grain rim but does not form a rind as Co and Ni do (Figure 9j). Concentric zonation bands are not uniform across the grain; they contain kinks and offsets that are more pronounced toward the margin of the grain (Figure 9). Cross-cutting the micron-scale concentric zonations is a diagonal zone 50–100  $\mu\text{m}$  wide containing randomly orientated Ni-rich, Se-poor pyrite with heterogeneous Co content (Figures 9i–9k). The contact with surrounding Se-enriched pyrite is sharp (Figure 9k).

#### 4.4. Bulk-Rock Geochemistry

Sample 357C has a notably higher Cu content relative to the other samples, it is also enriched in  $\text{TiO}_2$ . High  $\text{SiO}_2$ , MgO, and  $\text{Al}_2\text{O}_3$  indicate that the sample contained a higher proportion of wall-rock material, whereas elevated Fe and S content is consistent with increased hematite, magnetite and pyrite contents (Table 1). All samples returned Au and Ag contents below the detectable limit (Table 1). Samples contained high Co, Cr, and Ni contents and all other metals analyzed occurred in trace amounts <200 ppm (Table 1).

#### 4.5. Pyrite Geochemistry

Laser-ablation spot analyses confirm that pyrite contains high contents of Co and Ni with a median of 52.6 and 529 ppm ( $n = 168$ ), respectively (Figure 10a). Intragrain variation in Co content ranges from 67.9 to 2,907 ppm ( $n = 10$ ) and 64.5 to 6,973 for Ni ( $n = 19$ ). This confirms the highly heterogeneous Co and Ni distribution found during geochemical mapping (Figures 7–9). Copper contents were generally low with a median of 4.5 ppm ( $n = 168$ ); however, one grain did contain 12,126 ppm Cu (Figure 10a), having an irregular time resolved analysis profile indicating the presence of chalcopyrite inclusions. Selenium was detectable in 95% of samples with a median content of 6.5 ppm and maximum of 279 ppm ( $n = 168$ ). In one grain, the Se content varied from 0.80 to 101 ppm ( $n = 26$ ); however, in most samples, the Se content was less variable.

Manganese, Zn, As, and Te all occur in trace amounts with median contents ranging from 0.6 to 6.5 ppm (Figure 10b). There is no notable trend in their mineral-scale distribution (i.e., across individual grains). Vanadium, Cr, Pb and Bi all have median contents <1.2 ppm (Figure 10c); they are homogeneously distributed across the mineral grains analyzed. The median content of Ge, Ga, Mo, Sn and Au is <1 ppm, with many analyses below the detectable limit (Table S3 in Supporting Information S2) (Figure 10d). Pyrite is Au-poor with maximum content of 0.06 ppm and a median of 0.01 ppm ( $n = 50$ ), with only 30% of analyses above the detection limit.

There is no systematic relationship between the location of the analytical spot and Co or Ni content; the median Ni content of the pyrite cores is 344 ppm ( $n = 29$ ) versus 457 ppm ( $n = 34$ ) for the rim (Figure 10e). Tellurium and Se have median contents of 30 and 1.1 ppm in the core and 4.4 and 0.2 ppm at the grain rim (Figure 10f) and a moderate-to-strong correlation between Te and Se in the core ( $R^2 = 0.77$ ), and a moderate correlation at the rim ( $R^2 = 0.45$ ) is noted.

To assess intragrain variation in trace metal content, line analysis was performed. Line analysis confirms observations from element mapping and etching studies that the content of Ni and Co is highly variable across individual grains (Figure 11a). The distribution of Ni and Co broadly correlate with the grains; however, in some areas the enrichment of the two elements is offset (arrows in Figures 11a and 11b). Gold and Ag have irregular profiles occurring as discrete peaks (Figures 11a and 11b). In one pyrite grain, there is a strong correlation between Cu, Au and Ag (Figure 11b). Tellurium and Se exhibit similar co-variation (Figures 11a and 11b). Copper commonly has a flat ablation profile, with the exception of two discrete peaks in one pyrite grain (Figure 11b).

#### 4.6. Sulfur Isotopes

Six analytical transects ( $n = 45$  spots; Table 2) were conducted across different pyrite grains or sub-regions of the grain perpendicular to where zonations occur; the locations of analytical transects are shown in Figures 7–9.

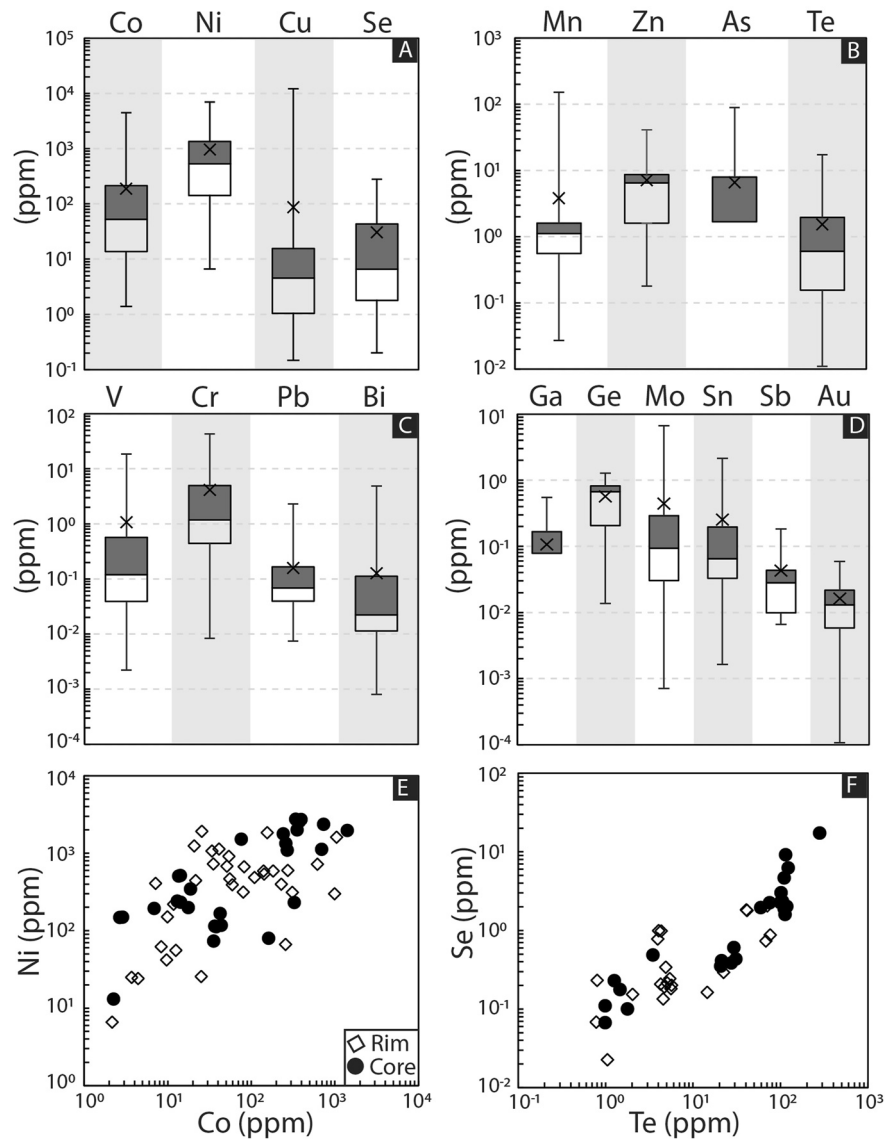


**Figure 10.** Summary plot of pyrite geochemistry analyzed via LA-ICP-MS ( $n = 168$ ). (a) Co, Ni, Cu and Se contents. (b) Mn, Zn, As, and Te contents. (c) V, Cr, Pb, and Bi contents. (d) Ga, Ge, Mo, Sn, Sb and Au content of pyrite. (e) Ni versus Co and (f) Se versus Te, classified by spot location into core/rim of grain. X = average, line = median, whiskers = min/max, boxes = upper and lower quartiles.

The average  $\delta^{34}\text{S}$  value for all samples is  $6.4 \pm 1.3\text{‰}$  ( $n = 45$ ,  $1\sigma$ ; Table 2). Intragrain variation is summarized in Figure 12. In all transects, the grain margin was enriched in  $^{34}\text{S}$  relative to the core, this is best observed in Figure 9k, where the margin of the grain has a  $\delta^{34}\text{S}$  value of  $9.2\text{‰}$  whilst all values within the core zone are  $<6.6\text{‰}$ . Similar trends were observed in all other grains we analyzed.

## 5. Discussion

### 5.1. Alteration Mineralogy and Mineral Paragenesis

The samples analyzed in this study show evidence of multiple temporally discrete hydrothermal mineralization events, indicating that they formed over a protracted period of time. We identify at least three discrete phases of mineralization but the temporal relationship between later events remains unclear. Chlorite-rich clasts that contain chalcopyrite (Figure 5k) indicate the presence of early chalcopyrite-rich veins, perhaps forming part of a basalt-hosted stockwork, that were later brecciated forming discrete chlorite  $\pm$  chalcopyrite-rich

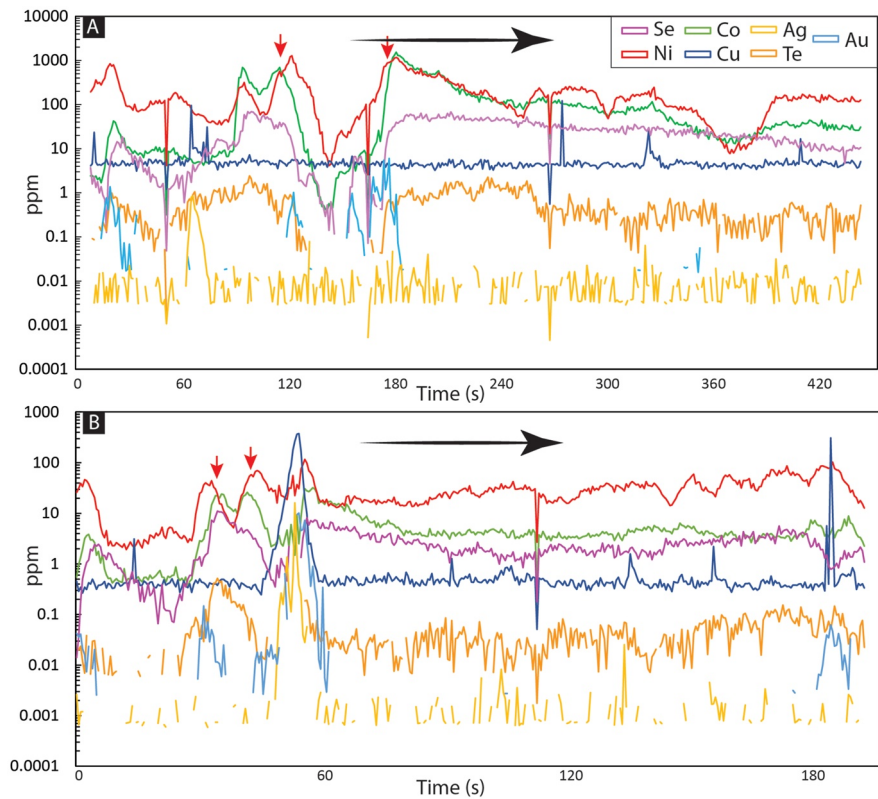


**Figure 11.** Time resolved analytical transect for pyrite (LA-ICP-MS). Transect locations are shown in Figure 3. (a) Trace metal content is highly variable across this large euhedral pyrite. Ni and Co content shows an order of magnitude variation with slight offsets in the enrichment profiles (red arrows), as observed in trace metal maps. Copper is homogeneously distributed, whereas Ag and Au have irregular profiles. Selenium exhibits some co variation with Ni and Co. (b) Nickel and Co are highly variable with a slight offset between the enrichment profiles. Copper occurs as discrete peaks that correlate with Ag and Au. Selenium exhibits some co variation with Ni, Co and Te. TRA profiles support the highly heterogeneous distribution of Ni, Co and Se observed in element maps. Black arrows indicate the direction of laser motion.

clasts. These clasts are then overprinted by two discrete vein networks; one rich in magnetite, pyrite and hematite (Figures 5g and 5h), the other containing predominantly quartz, apatite, pyrite and minor chalcopyrite (Figure 5l); however, there are no clear cross-cutting relationships between these two vein sets and it is unclear which formed first (Figures 3 and 4). We relate the multiple episodes of mineralization, vein formation and brecciation to changing fluid conditions in the active domain of the detachment fault, suggesting that samples likely formed at deeper crustal levels and were progressively exhumed over time (see Evidence of post-formation deformation).

Samples, that were likely basaltic in composition are altered to a mineral assemblage of chlorite, quartz, rutile and apatite with hematite, magnetite and pyrite (Figures 2 and 3). Chlorite occurs within sub-angular clasts that represent altered mafic wall-rock fragments and intergrown with quartz in a network of discrete veins (Figures 2 and 3). Chlorite forms at temperatures of  $>120^{\circ}\text{C}$  in near neutral pH fluids (Reyes, 1990) and is common in seafloor hydrothermal systems forming during the alteration of mafic host rocks by seawater derived hydrothermal fluids (Humphris & Thompson, 1978). Quartz forms at temperatures  $>150^{\circ}\text{C}$  and up to  $\sim 320^{\circ}\text{C}$ , from fluids with a low to near neutral pH (Reyes, 1990). In the samples analyzed, pyrite is spatially associated with networks of quartz veins that cross-cut chlorite-rich material (Figures 2 and 3). The intergrowth of quartz with chlorite and rutile indicates fluid temperatures of  $>180^{\circ}\text{C}$  (Reyes, 1990). The absence of minerals such as epidote and illite intergrown with chlorite limits the upper temperature of alteration to around  $300^{\circ}\text{C}$  (Reyes, 1990; Schiffman & Fridleifsson, 1991). Moreover, similar alteration mineral assemblages containing chlorite-rich silica breccias, comparable to those described here, have been sampled on the detachment surface at  $13^{\circ}20'N$  (Bonnemains et al., 2017; Verlaquet et al., 2021), suggesting this alteration mineral assemblage and the fluids from which it formed may be common amongst different detachment fault zones.

**Table 2**  
Sulfur Isotope Analysis of Individual Pyrite Grains From 13°30'N Analyzed Via SIMS ( $n = 45$ )

Pyrite grain	$\delta^{34}\text{S}$ (‰)
Grain 1 ( $n = 10$ )	
Average	6.2
Median	6.0
$\sigma$	1.1
Grain 2 ( $n = 5$ )	
Average	7.0
Median	7.4
$\sigma$	0.7
Grain 3 ( $n = 7$ )	
Average	7.9
Median	7.6
$\sigma$	0.6
Grain 4 ( $n = 5$ )	
Average	4.7
Median	4.4
$\sigma$	1.1
Grain 5 ( $n = 10$ )	
Average	6.5
Median	5.6
$\sigma$	1.4
Grain 6 ( $n = 8$ )	
Average	6.0
Median	5.9
$\sigma$	0.8
All analyses ( $n = 45$ )	
Average	6.9
Median	6.9
$\sigma$	1.1

Note. The location of analytical transects are shown in Figures 7–9.

The absence of any anhydrite, which is ubiquitous in many active SMS deposits (Petersen et al., 2000) in samples is due to its retrograde solubility in fluids <160°C (Blounot & Dickson, 1969), with similar anhydrite-poor alteration assemblages found in recently inactive hydrothermal systems such as the Brothers NW Caldera vent site (Martin et al., 2022a). The occurrence of microscopic apatite grains associated with quartz veins, as observed here, has not been documented in other SMS deposits. Given the association of apatite exclusively with quartz veins and not in chlorite-rich clast material, a hydrothermal origin is conceivable. Chrome spinel with Fe-rich alteration rims have been reported in other ultramafic-hosted SMS deposits, where spinel is inherited from ultramafic host rocks during replacement by secondary hydrothermal minerals (Borodaev et al., 2007; Fouquet et al., 2010; Marques et al., 2006). However, as chrome spinel occurs mainly within pyrite and quartz-hematite-magnetite veins (Figures 2 and 3), it may have formed during host rock replacement of an ultramafic protolith or have precipitated directly from the hydrothermal fluid (Huang et al., 2019). Thus, the origin of chrome spinel in 13°30'N samples remains enigmatic.

Hematite and magnetite were ubiquitous in all samples analyzed. The relationship between magnetite and hematite is not clear (Figures 4d–4f). In some grains hematite can be observed replacing euhedral magnetite grains (Figure 4d). Hematite can be a primary hydrothermal precipitate or produced by the oxidation of magnetite (Zhao et al., 2019), with both primary hydrothermal and secondary origin through the oxidation of magnetite suggested here. Regardless of the exact relationship, the presence of magnetite and hematite indicates the presence of oxidizing fluids. We suggest that decreasing fluid  $f\text{S}_2$  is less significant here relative to increasing  $f\text{O}_2$ , as pyrite is abundant and indicates relatively high fluid  $f\text{S}_2$ , hence we conclude that the magnetite and hematite formation occurred in response to increasing fluid  $f\text{O}_2$ .

The widespread occurrence of pyrite with discrete rims that are magnetite and hematite-rich relative to core zones indicates changes in fluid  $f\text{O}_2$ , and potentially a small decrease in  $f\text{S}_2$  over time (Kawasumi & Chiba, 2017; Ohmoto, 2003). We discount the direct oxidation of pyrite to hematite and magnetite as a major process based on the distribution of magnetite and hematite, that occur most prolifically in the sample matrix intergrown with quartz or as discrete overgrowth rims (Figures 3 and 4). If magnetite and hematite were directly formed from the oxidization of pyrite then they would be expected to preferentially occur within or be spatially associated with pyrite grains, and this is not the case (Figures 3 and 4).

Based on the relationship between the different alteration minerals present, a mineral paragenesis can be established. Mafic-ultramafic host rocks were altered to chlorite-rich assemblages by ascending hydrothermal fluids at temperatures between 180 and 300°C. A later episode of hydrothermal fluid flow at comparably high temperatures overprints wall-rock alteration forming a discrete network of quartz-pyrite-rich veins. Progressive growth of the quartz-pyrite vein networks replaced chlorite-rich wall-rock, possibly inheriting the contained chrome spinel grains that are more resistant to dissolution than the chlorite-rich matrix material. After the initial pyrite growth, which occurred under reduced fluid conditions at a moderately low pH, the redox of the fluid changed, leading to the precipitation of hematite and magnetite, or hematite that was replaced by magnetite, or vice versa, with these fluids exploiting the pre-existing permeability networks developed along the quartz-pyrite vein networks. The mineral paragenesis of samples indicates that at least three temporally distinct hydrothermal events occurred, with later fluids being more oxidizing and relatively depleted in  $\text{H}_2\text{S}$ .

Comparable mineral assemblages have been observed at the detachment-fault-hosted Suze vent field on the SWIR, where hematite and magnetite form a major mineral phase (20%–30% by volume; Liao et al., 2022). Quantitative mineralogy of samples at 13°30'N yielded similar results ranging from 20 to 22 wt.% Fe-oxide (Figures 2

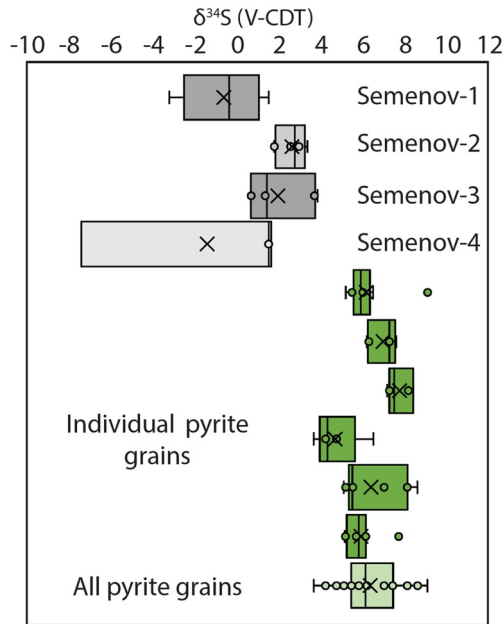


**Figure 12.** Sulfur isotope analysis of sulfide minerals from the Semenov vent field cluster (Melekestseva et al., 2014, 2017) and pyrite analyzed in this study ( $n = 45$ ). Pyrite from this study is enriched in  $^{34}\text{S}$  relative to other analyses at the seafloor in the Semenov vent field.

and 3). In contrast to samples at Suye that contain no chrome spinel grains, chrome spinel was an accessory phase ( $\sim 1$  wt.%) in our samples, indicating that clast material was possibly both ultramafic and mafic in origin at  $13^{\circ}30'\text{N}$  (Delacour et al., 2008; Marques et al., 2006). Alternatively, fluids were rich in Cr and capable of precipitating chrome spinel; however, this has not been documented in other systems and the solubility of Cr in hydrothermal fluids at temperatures of  $\sim 300^{\circ}\text{C}$  is low ( $< 5$  mg  $\text{kg}^{-1}$   $\text{H}_2\text{O}$ ; Huang et al., 2019). We suggest formation conditions similar to those estimated at Suye, with an oxygen fugacity higher ( $\log f\text{O}_2$   $-27$ ; Liao et al., 2022) than typical for most ultramafic and mafic-hosted vent fields ( $\log f\text{O}_2$   $\sim -33$  to  $-38$ ; Kawasumi & Chiba, 2017). Our mineralogical observations support the presence of oxidizing fluids in detachment fault zones on the Mid-Atlantic Ridge as previously found on the SWIR (Liao et al., 2022).

### 5.2. Evidence of an Ultramafic Metal Source

Ultramafic-influenced hydrothermal fields, where circulating hydrothermal fluid interacts with ultramafic rocks and fluids produced during serpentinization, produce geochemically distinct hydrothermal fluids and massive sulfide mineralization (Allen & Seyfried, 2003; Fouquet et al., 2010; Hannington et al., 2005; Kawasumi & Chiba, 2017). Hydrothermal fluids are more reducing relative to basalt-hosted environments (Figure 13) due to serpentinization reactions involving the hydration of olivine to form magnetite, silica and  $\text{H}_2$  (Allen & Seyfried, 2003). The resulting hydrothermal fluids in ultramafic-influenced vent sites can produce a mineral assemblage of magnetite, isocubanite and pyrrhotite (Borodaev et al., 2007; Marques et al., 2007;

Melekestseva et al., 2020). The occurrence of abundant magnetite in our samples supports the presence of highly reducing fluids that have been sampled in other ultramafic-hosted vent sites (Allen & Seyfried, 2003). However, the fact similar mineral assemblages have not been documented at the seafloor at  $13^{\circ}30'\text{N}$  (e.g., Semenov-3; Melekestseva et al., 2018), suggests the highly reducing fluids were not widespread.

Sulfide mineralization in ultramafic-influenced hydrothermal fields, and on-land VMS deposits are enriched in Ni, Co and platinum group elements relative to mafic-hosted environments (Hannington et al., 2005). The enrichment in Ni and Co is due to higher Ni and Co contents in ultramafic lithologies relative to mafic lithologies (Gale et al., 2013; Gülaçar & Delaloye, 1976). Bulk rock samples contain high Ni (up to 1,580 ppm; Table 1) and Co (up to 443 ppm), and provides evidence that fluids had interacted and leached metals from an ultramafic source lithology, located deeper in the system and therefore not accessible for sampling. The fluids then exploited the increased permeability associated with the detachment surface where they became mineralized at shallower crustal levels that are dominated by mafic lithologies, as observed in our samples. Pyrite from  $13^{\circ}30'\text{N}$  also contains high average Co and Ni contents at  $189 \pm 447$  and  $970 \pm 1,222$  ppm, respectively ( $1\sigma$ ,  $n = 168$ ), but the content is highly variable (Figure 10a). By comparison with sub-seafloor pyrite from the active TAG mound, a largely basalt hosted deposit has an average Co and Ni content of 448 and 22 ppm, respectively (Grant et al., 2018). Pyrite from ultramafic-hosted vent sites, such as Logachev and Kairei, contain comparably high Ni contents at 422 and 143 ppm, respectively (Keith, Haase, et al., 2016; Keith, Häckel, et al., 2016). Thus, the high average Ni content of pyrite at  $13^{\circ}30'\text{N}$  provides geochemical evidence that metals were contributed from an ultramafic source.

### 5.3. Metal Zonations in Pyrite

Two distinct types of zonation present in the samples analyzed intricate zonations ( $1\text{--}5$   $\mu\text{m}$ ) that are laterally continuous across individual grains, having a concentric zonation pattern emanating from the grain core, and irregular zonations that occur around areas of intragrain porosity or at the grain margin. The relationship between the two types of zonations is distinct; intricate zonations are overprinted by later irregular zonations. Concentric zonations, albeit of a less intricate nature, have been documented in several ore forming systems, for example, SMS deposits (Martin et al., 2023), epithermal Au deposits (Tanner et al., 2013, 2016) and porphyry Cu deposits (Reich et al., 2013). In these deposits, the concentric zonations are interpreted to be primary features that record

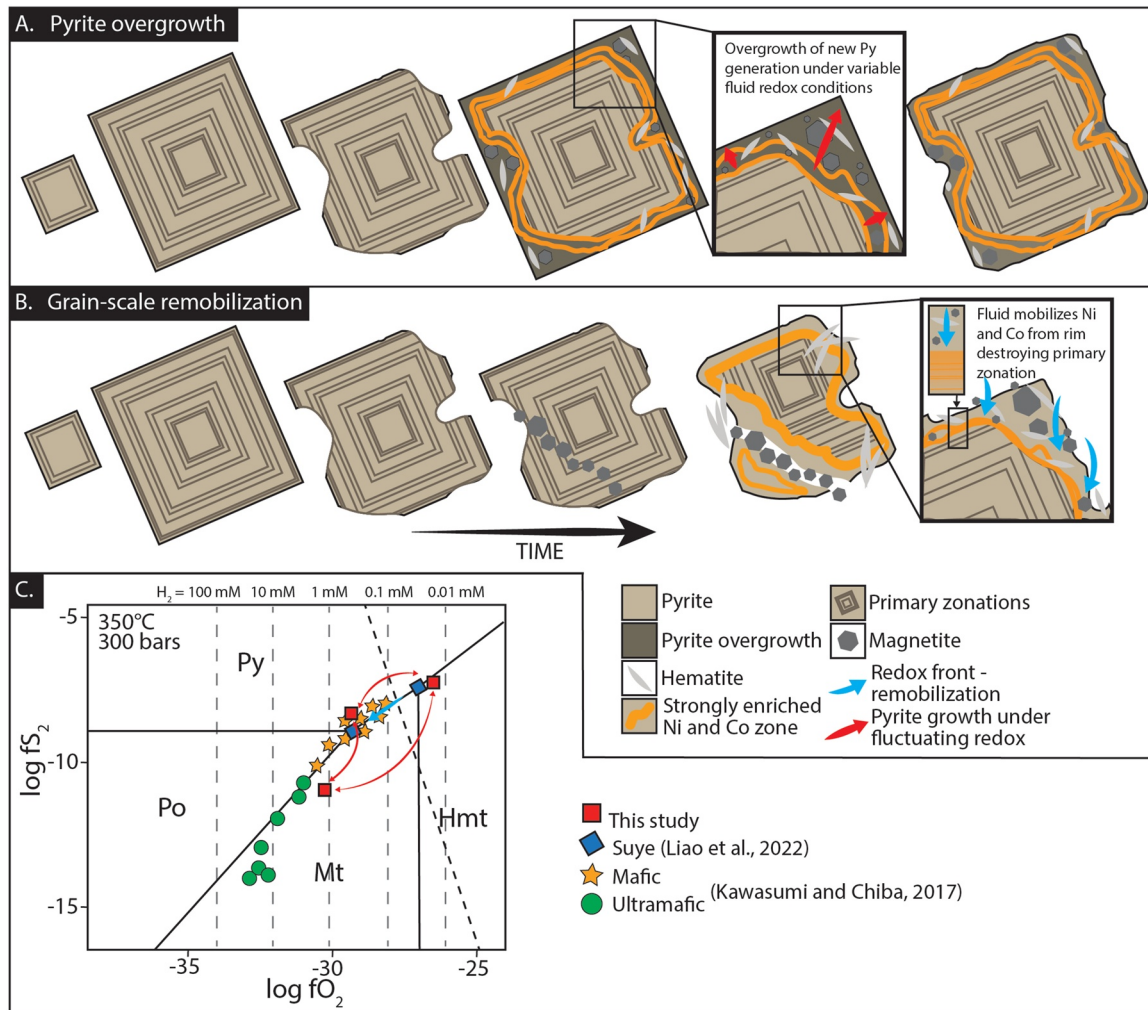


**Figure 13.** Summary schematic explaining the two possible origins of zonations in pyrite. (a) Pyrite overgrowth. Initially, pyrite forms with concentric zonations (primary) and has a euhedral morphology. Pyrite then undergoes dissolution during oxidation leading to a subhedral/anhydral morphology. The grain is then overgrown by a later pyrite generation with distinct pulses of Ni and Co-rich fluid under variable redox conditions forming rims that contain abundant hematite and magnetite (c). The grain then undergoes variable amounts of dissolution. (b) Grain-scale remobilization. Initially, pyrite forms euhedral grains with concentric primary zonations. During oxidation the grain undergoes dissolution forming subhedral/anhydral grains. Oxidizing fluids penetrate the grain along permeability structures precipitating magnetite and hematite. Nickel and Co are remobilized from the margin of the grain and permeability structure leading to the formation of Ni and Co reaction fronts that mark the extent to which fluids penetrated the pyrite grain. (c) Log  $f_{S_2}$ - $f_{O_2}$  diagram for the Fe-S-O system at 350°C and 300 bars (after Kawasumi & Chiba, 2017). Red squares show the approximate location of expected redox fluid conditions at 13°30'N. Arrows indicate that redox conditions fluctuated over time from the pyrite.

changes in the physicochemical conditions (e.g., pH, temperature, salinity) of the hydrothermal fluid that influences the solubility of different metals, that are subsequently recorded as variations in sulfide geochemistry as the grain grows. We interpret the fine-scale concentric zonations in pyrite from 13°30'N as primary features related to fluctuations in the chemistry and/or temperature of the hydrothermal fluid. To our knowledge, later overprinting of these primary features has not been observed in other SMS deposits, but we suggest that it may be a common phenomenon in deposits affected by later fluid flow events, where fluids had a distinctly different redox state. The distribution of irregular zonations along permeable horizons and near the grain margin indicates that they do not relate to primary compositional changes in hydrothermal fluid composition and are instead secondary.

Both primary and secondary zonations are most clearly distinguished by changes in Ni and Co content visible in element maps and in across grain time resolved analysis profiles (Figures 11a and 11b). Nickel and Co occur as  $Ni^{2+}$  and  $Co^{2+}$  that are substituted for  $Fe^{2+}$  in the pyrite crystal lattice (Huston, Sie, & Suter, 1995; Huston, Sie, Suter, Cooke, & Both, 1995; Maslennikov et al., 2009). Both Ni and Co commonly form concentric zonation patterns in pyrite in a range of different ore deposit types (e.g., IOCG, IOA; Steadman et al., 2021). Selenium

is also incorporated in a solid solution in the pyrite lattice by substituting for  $S^{2-}$  (Huston, Sie, & Suter, 1995; Huston, Sie, Suter, Cooke, & Both, 1995). In SMS deposits, Co, Ni and Se have an affinity for higher temperature fluids ( $>300^{\circ}\text{C}$ ), for example, at the active TAG mound, where they are enriched in pyrite from the stockwork and lower mound area (Grant et al., 2018). More recently, the importance of oxidized brines in the transport of Ni and Co has been investigated, showing that large quantities of both Ni and Co can be transported in both high-temperature ( $>250^{\circ}\text{C}$ ) low-pH hydrothermal fluids and near-neutral pH oxidized brines (Jansson & Liu, 2020). Cobalt is transported as  $\text{CoCl}_2(\text{H}_2\text{O})$  or  $\text{CoCl}_4^-$  (at  $150^{\circ}\text{C}$  and  $250^{\circ}\text{C}$ , respectively), whereas Ni is transported as  $\text{NiCl}_2$  at both  $150$  and  $250^{\circ}\text{C}$  (Jansson & Liu, 2020). Jansson and Liu (2020) show that Co is soluble at any pH at  $150^{\circ}\text{C}$ , whereas Ni is insoluble at a pH above 7. Thus, the difference in the distribution of Ni and Co can be explained as a function of fluctuating fluid pH, with Ni being insoluble when the fluid pH was above 7. Moreover, Maslennikov et al. (2009) note that increasing  $fS_2$  or decreasing temperature first favors the substitution of  $\text{Co}^{2+}$  followed by  $\text{Ni}^{2+}$  for  $\text{Fe}^{2+}$  in the pyrite crystal lattice. Therefore, Co and Ni distribution in pyrite is affected by varying relative contributions of geochemically distinct fluids, namely ambient seawater and high-temperature ( $>250^{\circ}\text{C}$ ) and acidic hydrothermal fluid. A relatively higher influx of hydrothermal fluid would decrease the fluid  $fO_2$ , increase  $fS_2$  and increase temperature, whereas seawater influx would have the opposite effect.

When considering primary concentric zonations, Se is enriched between the zones of Co and Ni enrichment (Figures 8h–8l and 9a–9j). This indicates a decoupled relationship between Se and Ni-Co. Selenium-rich zones could have formed from several processes: magmatic degassing episodes, as Se has an affinity for the volatile phase (Martin et al., 2021), variations in fluid redox, with oxidized fluids being able to transport higher amounts of Se (Huston et al., 1995a, 1995b), or pulses of higher temperature fluid, as Se is preferentially enriched in high-temperature pyrite generations (Butler & Nesbitt, 1999).

At the active TAG mound, Se, Co and Ni are co-enriched in sub-seafloor pyrite (Grant et al., 2018), due to their affinity for high-temperature hydrothermal fluids. In contrast, Revan et al. (2014) found a decoupled relationship between Se, Co and Ni across individual chimney conduits, related to the increased solubility of Ni in moderate to high-temperature fluids, leading to Ni precipitation at relatively low temperatures compared with Co and Se. Our data is consistent with this observation, showing that the metal behavior and enrichment processes that occur at the chimney scale also apply at the scale of individual mineral grains.

The addition of Se during magmatic volatile degassing may also be important in controlling the mineral-scale distribution of Se, as previous studies have suggested that some metals in the Semenov vent cluster (e.g., Au, Ag, Te, Se) were contributed by magmatic volatile degassing (Melekestseva et al., 2017). However, Se enriched zones in our samples do not correlate with decreasing  $\delta^{34}\text{S}$  values (Figures 8l and 9k), and  $\delta^{34}\text{S}$  values  $< 0\text{‰}$  are absent, which does not support the presence of an  $\text{SO}_2$ -rich magmatic volatile phase (e.g., Herzig et al., 1998).

#### 5.4. Origin of Secondary Zonations: Remobilization or Overgrowth?

All of the pyrite grains that we examined show distinct zonation patterns: Ni and Co (+Se) are depleted at the grain margin ( $\sim 10\text{--}50\ \mu\text{m}$  wide) and in the center of grains surrounding inclusion-rich or porous regions, and are mantled by zones of Ni and Co enrichment forming a thin rind ( $\sim 1\text{--}5\ \mu\text{m}$  wide; e.g., Figures 3e–3g). There are two hypotheses that can explain the distribution of Ni and Co and textural observations in our samples: (a) the Ni-Co (+Se) depleted zone at the grain margin is a new generation of pyrite overgrowth precipitated under distinct conditions from a fluid that was relatively depleted in Ni and Co, or (b) Ni and Co were remobilized from surrounding permeable regions and the grain margin by later chemically distinct fluids, but pyrite did not undergo dissolution and reprecipitation (Bente & Doering, 1995).

Some pyrite grains have an anhedral morphology or resorbed core with the margin of the grain exhibiting a depletion in Ni and Co (e.g., Figures 9g–9k). The pyrite grain margins commonly contain numerous hematite and magnetite inclusions that decrease in abundance toward the grain core (e.g., Figures 7g–7l). In our first hypothesis, pyrite undergoes a phase of dissolution, most likely due to oxidation driven by prolonged periods of seawater ingress, and is then overprinted by a later pyrite generation that formed during a renewed phase of hydrothermal activity (Figure 13a). Dissolution and reprecipitation effectively explain the sharp boundaries between primary concentric zonations, the generally irregular shape of this boundary, representing the anhedral pyrite grain after oxidation and dissolution, and the precipitation of a later pyrite generation that is relatively depleted in Ni and Co and does not contain primary concentric zonations. The pyrite overgrowth formed from geochemically distinct

fluids that did not contain high Co, Ni or Se, most likely due to lower fluid temperatures, low H<sub>2</sub>S contents, and higher *f*O<sub>2</sub>, forming magnetite and hematite-rich rims in some pyrite grains (Figures 4d–4f).

However, the dissolution followed by reprecipitation of pyrite (Figure 13a) cannot explain some of the more complex textural features, such as “channel structures” (Figures 9a–9f), frilly and intricate metal enrichment zones (Figures 8a–8f), and the occurrence of Co and Ni enriched zones away from the grain margin where overgrowth is expected to occur (Figures 8g–8l). Thus, we suggest that secondary zonations of Ni and Co do not solely represent dissolution and reprecipitation reactions, instead indicating that redistribution of trace metals has occurred due to fluid overprinting where the pyrite grain did not undergo dissolution. Oxidizing fluids (Figure 13c) reacted with pyrite leading to the solid-state (i.e., coupled dissolution-reprecipitation reactions; Ruiz-Agudo et al., 2014) remobilization and concentration of Ni and Co. Similar diffusion process can influence Cu and In distribution in sphalerite (Bente & Doering, 1995), however experimental data characterizing the diffusion of elements in pyrite remains undetermined. Diffusion and remobilization occurred both at the grain margin and within permeable regions in the grain interior (Figure 13b). Permeability networks within pyrite were created during pyrite dissolution and can be seen as orientated networks of vugs or inclusions of magnetite/hematite indicating fluid flow (e.g., Figures 4d, 4e, and 8h).

The overprinting fluid erases primary textural features such as concentric zonations and concentrates metals along reaction fronts (Figures 8b and 8e; Figure 13b). The reaction front, enriched in Ni and Co, defines the limit that fluids penetrated the pyrite grain. Remobilization best explains the occurrence of intricate “channel structures” where primary zonations in Co, Ni, and Se are disrupted and erased (Figures 9d–9f), in close proximity to areas of magnetite formation. The zonations in the channel structures have a shadow or tail structure that disrupts the concentric zonation, representing directional fluid flow from a zone of increased permeability (Figure 9b). The localized disruption of primary zonations indicates that remobilization at the mineral-scale was extensive and did not occur only at the grain margin (e.g., Figures 8h, 8j, and 8k). Thus, the mineral-scale distribution of metals is influenced by both dissolution-reprecipitation reactions and fluid overprinting that led to the solid-state remobilization and concentration of metals (Figure 13).

Numerous studies have documented the remobilization of trace metals in seafloor hydrothermal systems (Evans et al., 2020; Gallant & Von Damm, 2006; Keith, Häckel, et al., 2016; Martin et al., 2022b), however, what is generally assumed that complete dissolution of the mineral or part of the mineral occurs and is followed by either the precipitation of a secondary mineral phase or loss of a given metal from the system in the fluid phase (e.g., Haymon, 1983). The remobilization of trace metals can also occur due to galvanic interactions between different sulfide minerals during oxidation, where two minerals with different rest potentials in an electrolyte solution act as a cathode (e.g., pyrite) and anode (e.g., chalcopyrite) (Abraitis et al., 2004; Fallon et al., 2017). Here, we provide microtextural and geochemical evidence of an additional mechanism of trace metal enrichment where metals are remobilized at the scale of individual mineral grains, and, in the case of Ni and Co, may become concentrated and not lost to the fluid phase during mineral dissolution. In contrast, Se is not enriched at the reaction fronts, indicating that it is lost from the system. However, an effective mechanism explaining the solid-state remobilization or perhaps diffusion of Ni and Co, without dissolution and reprecipitation in pyrite due to fluctuating redox conditions remains enigmatic, though the textural evidence supporting this process is clear.

The sulfur isotopic composition of pyrite provides further complimentary evidence for changes in the source of the hydrothermal fluid as the pyrite grains grew (Figures 7–9). In SMS deposits, and associated hydrothermal systems, sulfur is principally sourced via thermochemical sulfate reduction (TSR) of seawater (~21‰; Rees et al., 1978) and the leaching of sulfur from oceanic lithosphere and contained magmatic sulfide minerals (~0‰; Sakai et al., 1984). This two component mixing forms sulfide minerals in sediment-free MOR Setting with δ<sup>34</sup>S values of between 0 and 5‰ (e.g., Hannington et al., 2005). The addition of sulfur from SO<sub>2</sub> degassing, where SO<sub>2</sub> undergoes disproportionation, typical of subduction-influenced vent sites, produces a more variable sulfur isotopic signature in sulfide minerals, typically with δ<sup>34</sup>S values of <0‰ (de Ronde et al., 2011; Herzig et al., 1998; Petersen et al., 2002).

Previous investigations utilizing sulfur isotope ratios of sulfide minerals at Semenov -1, -2, -3 and -4 have an average δ<sup>34</sup>S value of 0.9 ± 2.5‰ (*n* = 25, 1σ) (Figure 12). Notably, several δ<sup>34</sup>S values at Semenov-1 plot at <0‰, and, coupled with an enrichment of Au and Ag in the nearby Semenov-2 vent field, are interpreted as evidence of magmatic volatile influx (Melekestseva et al., 2014, 2017). Our data from the exposed fault surface at Semenov-4 does not support the presence of a magmatic volatile phase, indicating that if a magmatic volatile

phase was present in the Semenov vent field cluster, it was a localized phenomenon, both temporally and spatially (Herzig et al., 1998; Martin et al., 2021). The average  $\delta^{34}\text{S}$  value for all analyses in this study is consistent with the contribution of sulfur from TSR and the leaching of host rocks at  $6.4 \pm 1.3\%$  ( $n = 45$ ,  $1\sigma$ ). However, systematic variations in  $\delta^{34}\text{S}$  values across several pyrite grains indicate temporal variability in the source of sulfur or fluid conditions during pyrite growth (Figures 7–9).

In all grains analyzed, the rim of the grain was enriched in  $^{34}\text{S}$  relative to the core. For example, the margin of the grain in one sample (Figure 8h), where secondary zonations occur, consistently contained  $\delta^{34}\text{S}$  values  $> 8\%$  ( $n = 3$ ), that decreased sharply from 8.7 to 5.2‰ toward the center of the grain where primary zonations were present. A similar trend where  $\delta^{34}\text{S}$  values decrease from 9.2‰ in secondary zonations to 5.3‰ across primary zonations occurred in another grain (Figure 9). A similar range in  $\delta^{34}\text{S}$  values has been reported in other detachment fault-related vent sites such as Suye, where increasing  $\delta^{34}\text{S}$  values from 4.4 to 11.3‰ in sulfide minerals indicates an increase in the amount of sulfur derived from TSR of seawater from ~36% to ~50% (Liao et al., 2022). Assuming that seawater sulfate is quantitatively reduced to sulfide, and a two-component mixing model is valid, then:  $\delta^{34}\text{S}_{\text{mix}} = X * \delta^{34}\text{S}_{\text{Seawater}} + (1 - X) * \delta^{34}\text{S}_{\text{Basalt}}$ , where seawater = ~21‰ (Rees et al., 1978), basalt = 0.1‰ (Sakai et al., 1984), and “X” represents the amount of sulfate contributed from TSR of seawater. Then the amount of sulfur derived from TSR of seawater at 13°30'N ranged from 18% to 43%, with an average for all analyses of 30%. This range is in good agreement with values reported at the Suye hydrothermal field (Liao et al., 2022), with the average value at 13°30'N comparable to sediment-free SMS/VMS deposits ranging from 0% to 33% (Keith, Haase, et al., 2016; Martin et al., 2019; Zeng et al., 2017). We show that the same systematic variation in  $\delta^{34}\text{S}$  values as observed using micro-drilling of sulfide minerals at Suye also occurs at the micron-scale across individual mineral grains. In pyrite rims at 13°30'N, high  $\delta^{34}\text{S}$  values ( $>8\%$ ) represent an increase in the amount of sulfur sourced from the TSR of seawater. The lower  $\delta^{34}\text{S}$  values preserved in the grain core, where primary zonations are present, indicating that a higher proportion of sulfur was leached from host rocks leading to lower  $\delta^{34}\text{S}$  values, which are typical of many SMS deposits (Zeng et al., 2017).

As previously discussed, some pyrite grains did not undergo dissolution but instead were overprinted by an oxidizing fluid. If this is the case, then it suggests that  $^{32}\text{S}$  has been preferentially remobilized relative to  $^{34}\text{S}$  producing high  $\delta^{34}\text{S}$  values in pyrite. Diffusion is one possible mechanism where pyrite would react with surrounding fluids that had a higher  $^{34}\text{S}/^{32}\text{S}$  ratio than earlier formed pyrite, due to increased seawater influx, however, diffusion requires high-temperatures ( $\gg 200^\circ\text{C}$ ) and occurs on a timescale of millions to 10s of millions of years (Watson et al., 2009). Therefore, the diffusion of sulfur does not provide a plausible mechanism to explain the distribution of sulfur isotope values at 13°30'N, as the OCC is estimated to be only 470,000 years old (Escartín et al., 2017), and sulfide mineralization on the seafloor is younger still (max 124,000 years; Kuznetsov et al., 2011). Coupled with the relatively low temperatures ( $<350^\circ\text{C}$ ) derived from the alteration mineral assemblage, diffusion is unlikely to alter the sulfur isotopic composition of pyrite. Hence, we cannot fully reconcile our textural observations with isotopic or geochemical signatures.

### 5.5. Significance of Fluctuating Redox Conditions

We show here that fluctuating fluid redox plays an important role in the concentration of trace metals across individual mineral grains (Figure 13c). At 13°30'N, episodes of seawater influx followed by renewed hydrothermal activity led to changes in fluid temperature, pH, and  $f\text{O}_2$  over time. During seawater ingress associated with prolonged fault movement along the detachment surface fluids became cooler (but still above 160°C to facilitate TSR; Machel et al., 1995), had a near neutral pH and were more oxidizing. Samples recovered from 13°30'N represent the transition from a typical high-temperature, reduced and sulfur-rich “black smoker” type fluid (Allen & Seyfried, 2003; Von Damm, 1990) to one dominated by seawater (Figure 13c). Microtextural evidence indicates that this transition concentrates metals in pyrite and that they are not lost from the system to the fluid, suggesting that recently active hydrothermal fields, prior to complete oxidation, can concentrate certain metals, especially redox-sensitive metals such as Ni and Co. Key questions remain if this process applies to black smoker chimneys and not only samples that once formed below the seafloor, as analyzed here, or ultramafic-hosted settings more widely, or if metal remobilization takes place under a unique set of fluid conditions found only at 13°30'N.

### 5.6. Evidence of Pyrite Deformation

Textural features within pyrite grains at 13°30'N have, to our knowledge, not been documented previously in VMS or SMS deposits. These are “streaky fabrics” (Figures 3g and 3h), “kink bands” (Figures 3j and 3k), “channel structures” (Figure 3l) and “mineral-scale deformation zones” (Figure 9h). The origin of some of these microtextural features is hard to comprehend without some degree of late-stage modification, deformation or remobilization, whether that is by late-stage fluid flow (e.g., channel structures) or due to lattice deformation/fracturing of the pyrite grains (e.g., kink bands and mineral-scale deformation zones; Figure 9h), or perhaps a combination of many different processes (e.g., streaky fabric; Figures 6g and 6h). But given that pyrite is more stable during metamorphism and reacts in a brittle manner compared with other sulfide minerals (Lafrance et al., 2020), it may record not only chemical compositional changes during primary hydrothermal processes but also later metamorphic events, in this case relating to slip along the detachment fault surface. A similar model is hypothesized at the 13°20'N OCC, where basaltic and rare ultramafic hydrothermally altered and silicified clasts, similar to those observed here, are brecciated and integrated along the detachment fault surface from a depth of 1–2 km, representing the base of the sheeted dyke complex in the hangingwall of the detachment (Bonnemains et al., 2017; Verlaquet et al., 2021).

Thus, the deformation structures in pyrite are consistent with the formation of samples at deeper crustal levels (possibly 1–2 km deep) below the seafloor where samples were progressively exhumed along a fault surface to their current location at the seafloor within the fault surface, which would have formed under the rift valley floor when the detachment was active, hence supporting the findings of Bonnemains et al. (2017) at the 13°20'N OCC. The formation of samples at deeper levels is further supported by early generations of brecciated basaltic clasts, multiple phases of vein growth, the large grain size of pyrite (several mm in some cases) and microtextural observations in pyrite such as grain scale deformation zones and kink bands.

The link between deformation and sulfide geochemistry remains a key area of research, especially given that many world-class VMS deposits (e.g., Kidd Creek, Canada) are located in greenschist facies metamorphic terranes where post-formation deformation is likely to occur and may lead to the remobilization of metals (e.g., Denisova et al., 2023). To further investigate these features and to understand the influence of pyrite deformation on trace metal distribution in SMS/VMS deposits and ore deposits more widely, a combined geochemical and microstructural approach using electron backscatter diffraction (EBSD) and geochemistry is needed.

## 6. Summary and Conclusion

We utilize a combined microtextural, geochemical and isotopic analytical approach with micron-scale resolution to investigate pyrite in an oxidizing detachment fault hosted environment. Samples analyzed from 13°30'N on the Mid-Atlantic Ridge contained pyrite, magnetite and hematite, indicating the presence of oxidizing fluids. Mafic-dominated lithologies, possibly containing ultramafic components that were progressively replaced by quartz-hematite-magnetite-pyrite vein networks, indicating fluid temperatures of ~250°C. Periods of pulsed seawater ingress due to ongoing fault movement along the detachment surface produced oxidizing fluids and led to the redistribution of Ni and Co at the scale of individual mineral grains. Our data provide evidence of trace metal behavior in response to fluctuating fluid redox, providing an analog to understand the waning stages of hydrothermal activity in SMS deposits and metal enrichment processes in detachment-fault hosted ultramafic environments. Later, deformation of pyrite that occurs as kink bands and micron-scale deformation zones indicates that pyrite formed ~1–2 km below the seafloor and was then exhumed along the detachment fault surface to its current position on a fault scarp at the seafloor.

Microtextural evidence shows that both primary and secondary zonations exist in pyrite at 13°30'N. Primary zonations occur on the micron scale, exhibit a concentric zonation pattern and are overprinted by secondary zonations. Secondary zonations are characterized by frilly, intricate, irregular zonation patterns and are spatially related to the grain margin or areas of high permeability within the grain core. In primary zonations, Se shows a decoupled relationship with Ni and Co. Primary zonations formed in response to fluctuating fluid redox and temperature variations during pyrite growth. The distribution of Ni and Co differs slightly due to the subtle difference in depositional efficiency related to changing temperature and pH between the two elements. The relationship between primary and secondary zonations is unambiguous; secondary zonations are later and overprint primary zonations. We propose two mechanisms explaining the observed textural and geochemical data: (a)

pyrite dissolution followed by re-precipitation of pyrite, and (b) the solid-state remobilization of trace metals by overprinting fluids forming metal enriched zones along redox fronts. These two processes are not mutually exclusive, and the mechanism varies between grains; however, the microtextural features such as frilly and irregular zonations and channel flow structures that have not been documented previously cannot be explained solely by the dissolution and reprecipitation of pyrite.

The sulfur isotopic ratio of pyrite does not support the presence of a prominent magmatic volatile phase as values <0‰ are absent. Sulfur is derived from the TSR of seawater and the leaching of igneous host rocks. Systematic analytical transects across the boundary between primary and secondary zonations indicate a change in the source of sulfur. The grain rim is systematically enriched in <sup>34</sup>S relative to the grain core, indicating that either later fluids that precipitated pyrite contained an increased proportion of sulfur sourced from TSR of seawater or that <sup>32</sup>S was preferentially remobilized during fluid overprinting and solid-state remobilization. Our data link the geochemical and isotopic composition of pyrite to the exhumation history of an oceanic detachment fault.

### Conflict of Interest

The authors declare no conflicts of interest relevant to this study.

### Data Availability Statement

All data related to this research are available at Martin (2023).

### References

- Abraitis, P. K., Patrick, R. A. D., & Vaughan, D. J. (2004). Variations in the compositional, textural and electrical properties of natural pyrite: A review. *International Journal of Mineral Processing*, 74(1–4), 41–59. <https://doi.org/10.1016/j.minpro.2003.09.002>
- Allen, D. E., & Seyfried, W. E. (2003). Compositional controls on vent fluids from ultramafic-hosted hydrothermal systems at mid-ocean ridges: An experimental study at 400°C, 500 bars. *Geochimica et Cosmochimica Acta*, 67(8), 1531–1542. [https://doi.org/10.1016/S0016-7037\(02\)01173-0](https://doi.org/10.1016/S0016-7037(02)01173-0)
- Almodóvar, G. R., Yesares, L., Sáez, R., Toscano, M., González, F., & Pons, J. M. (2019). Massive sulfide ores in the Iberian pyrite belt: Mineralogical and textural evolution. *Minerals*, 9(11), 653. <https://doi.org/10.3390/min9110653>
- Bente, K., & Doering, T. (1995). Experimental studies on the solid state diffusion of Cu + In in ZnS and on “disease,” DIS (diffusion induced segregations), in sphalerite and their geological applications. *Mineralogy and Petrology*, 53(4), 285–305. <https://doi.org/10.1007/BF01160153>
- Blounot, C. W., & Dickson, F. W. (1969). The solubility of anhydrite (CaSO<sub>4</sub>) in NaCl-H<sub>2</sub>O from 100 to 450°C and 1 to 1000 bars. *Geochimica et Cosmochimica Acta*, 33(2), 227–245. [https://doi.org/10.1016/0016-7037\(69\)90140-9](https://doi.org/10.1016/0016-7037(69)90140-9)
- Bonnemains, D., Escartin, J., Mevel, C., Andreani, M., & Verlaquet, A. (2017). Pervasive silicification and hanging wall overplating along the 13°20′ N oceanic detachment fault (Mid-Atlantic Ridge). *Geochemistry, Geophysics, Geosystems*, 18(6), 2028–2053. <https://doi.org/10.1002/2017GC006846>
- Borodav, Y. S., Bryzgalov, I. A., Mozgova, N. N., & Uspenskaya, T. Y. (2007). *Pentlandite and Co-enriched pentlandite as characteristic minerals of modern hydrothermal sulfide mounds hosted by serpentinized ultramafic rocks (Mid-Atlantic Ridge)* (Vol. 62, pp. 85–97). Moscow University Geology Bulletin. <https://doi.org/10.3103/S0145875207020032>
- Butler, I. B., & Nesbitt, R. W. (1999). Trace element distributions in the chalcopyrite wall of a black smoker chimney: Insights from laser ablation inductively coupled plasma mass spectrometry (LA-ICP-MS). *Earth and Planetary Science Letters*, 167(3–4), 335–345. [https://doi.org/10.1016/S0012-821X\(99\)00038-2](https://doi.org/10.1016/S0012-821X(99)00038-2)
- Cherkashev, G. A., Ivanov, V. N., Bel'tenev, V. I., Lazareva, L. I., Rozhdestvenskaya, I. I., Samovarov, M. L., et al. (2013). Massive sulfide ores of the northern equatorial Mid-Atlantic Ridge. *Oceanology*, 53(5), 607–619. <https://doi.org/10.1134/S0001437013050032>
- Crowe, D. E., & Vaughan, R. G. (1996). Characterization and use of isotopically homogeneous standards for in situ laser microprobe analysis of <sup>34</sup>S/<sup>32</sup>S ratios. *American Mineralogist*, 81(1–2), 187–193. <https://doi.org/10.2138/am-1996-1-223>
- Dekov, V. M., Garbe-Schönberg, D., Kamenov, G. D., Guéguen, B., Bayon, G., Bindi, L., et al. (2018). Redox changes in a seafloor hydrothermal system recorded in hematite-chalcopyrite chimneys. *Chemical Geology*, 483, 351–371. <https://doi.org/10.1016/j.chemgeo.2018.02.041>
- Delacour, A., Früh-Green, G. L., Bernasconi, S. M., & Kelley, D. S. (2008). Sulfur in peridotites and gabbros at Lost City (30°N, MAR): Implications for hydrothermal alteration and microbial activity during serpentinization. *Geochimica et Cosmochimica Acta*, 72(20), 5090–5110. <https://doi.org/10.1016/j.gca.2008.07.017>
- Denisová, N., Piercey, S. J., & Wälle, M. (2023). Mineralogy and mineral chemistry of the ABM replacement-style volcanogenic massive sulfide deposit, Finlayson Lake district, Yukon, Canada. *Mineralium Deposita*. <https://doi.org/10.1007/s00126-023-01217-4>
- de Ronde, C. E. J., Massoth, G. J., Butterfield, D. A., Christenson, B. W., Ishibashi, J., Ditchburn, R. G., et al. (2011). Submarine hydrothermal activity and gold-rich mineralization at brothers volcano, Kermadec arc, New Zealand. *Mineralium Deposita*, 46(5–6), 541–584. <https://doi.org/10.1007/s00126-011-0345-8>
- Escartin, J. (2014). ODEMAR oceanic detachment faults at the Mid-Atlantic Ridge. In *Cruise report. N/O Pourquoi pas? ROV victor 6000—AUV Abyss 6000. 16 November–19 December 2013, Mindelo (Cape Verde)—Point a Pitre (Guadeloupe)*. <https://doi.org/10.13155/47149>
- Escartin, J., Mével, C., Petersen, S., Bonnemains, D., Cannat, M., Andreani, M., et al. (2017). Tectonic structure, evolution, and the nature of oceanic core complexes and their detachment fault zones (13°20′N and 13°30′N, Mid Atlantic Ridge). *Geochemistry, Geophysics, Geosystems*, 18(4), 1451–1482. <https://doi.org/10.1002/2016GC006775>
- Escartin, J., & Petersen, S. (2017). ODEMAR AUV Abyss (GEOMAR) + shipboard Pourquoi Pas? Multibeam bathymetry—13deg20′N and 13deg30′N oceanic core complexes. *Mid Atlantic Ridge*. <https://doi.org/10.17882/48335>

### Acknowledgments

We thank the Captain and crew aboard the N/O *Pourquoi Pas?* and ROV Victor6000 crew. The ODEMAR cruise and project were supported by CNRS and the Flotte Océanographique Française (France). Wanda Aylward is thanked for her assistance during EPMA map acquisition, Marcus Wälle during LA-ICP-MS mapping and Ryan Sharpe during SIMS analysis. Jamieson acknowledges the support of the Canada Research Chair program. We thank Whitney Behr for the editorial handling of this manuscript and Andrew McCaig and an anonymous reviewer for their thoughtful reviews. The publication fees for this article were supported by the UNLV University Libraries Open Article Fund.

- Evans, G. N., Tivey, M. K., Monteleone, B., Shimizu, N., Seewald, J. S., & Rouxel, O. J. (2020). Trace element proxies of seafloor hydrothermal fluids based on secondary ion mass spectrometry (SIMS) of black smoker chimney linings. *Geochimica et Cosmochimica Acta*, 269, 346–375. <https://doi.org/10.1016/j.gca.2019.09.038>
- Fallon, E. K., Petersen, S., Brooker, R. A., & Scott, T. B. (2017). Oxidative dissolution of hydrothermal mixed-sulphide ore: An assessment of current knowledge in relation to seafloor massive sulphide mining. *Ore Geology Reviews*, 86, 309–337. <https://doi.org/10.1016/j.oregeorev.2017.02.028>
- Fouquet, Y., Cambon, P., Etoubleau, J., Charlou, J. L., Ondréas, H., Barriga, F. J. A. S., et al. (2010). Geodiversity of hydrothermal processes along the Mid-Atlantic Ridge and ultramafic-hosted mineralization: A new type of oceanic Cu-Zn-Co-Au volcanogenic massive sulfide deposit. In P. A. Rona, C. W. Devey, J. Dymant, & B. J. Murton (Eds.), *Geophysical monograph series* (Vol. 188, pp. 321–367). American Geophysical Union. <https://doi.org/10.1029/2008GM000746>
- Gale, A., Dalton, C. A., Langmuir, C. H., Su, Y., & Schilling, J.-G. (2013). The mean composition of ocean ridge basalts. *Geochemistry, Geophysics, Geosystems*, 14(3), 489–518. <https://doi.org/10.1029/2012GC004334>
- Gallant, R. M., & Von Damm, K. L. (2006). Geochemical controls on hydrothermal fluids from the Kairei and Edmond vent fields, 23°–25°S, Central Indian ridge. *Geochemistry, Geophysics, Geosystems*, 7(6), Q06018. <https://doi.org/10.1029/2005GC001067>
- Grant, H. L. J., Hannington, M. D., Petersen, S., Frische, M., & Fuchs, S. H. (2018). Constraints on the behavior of trace elements in the actively-forming TAG deposit, Mid-Atlantic Ridge, based on LA-ICP-MS analyses of pyrite. *Chemical Geology*, 498, 45–71. <https://doi.org/10.1016/j.chemgeo.2018.08.019>
- Gülaçar, O. F., & Delaloye, M. (1976). Geochemistry of nickel, cobalt and copper in alpine-type ultramafic rocks. *Chemical Geology*, 17, 269–280. [https://doi.org/10.1016/0009-2541\(76\)90041-3](https://doi.org/10.1016/0009-2541(76)90041-3)
- Haase, K. M., Petersen, S., Koschinsky, A., Seifert, R., Devey, C. W., Keir, R., et al. (2007). Young volcanism and related hydrothermal activity at 5°S on the slow-spreading southern Mid-Atlantic Ridge. *Geochemistry, Geophysics, Geosystems*, 8(11). <https://doi.org/10.1029/2006GC001509>
- Hannington, M. D., de Ronde, C. D. J., & Petersen, S. (2005). Sea-floor tectonics and submarine hydrothermal systems. In J. W. Hedenquist, J. F. H. Thompson, R. J. Goldfarb, & J. P. Richards (Eds.), *Economic geology 100th anniversary volume* (pp. 111–141). Society of Economic. <https://doi.org/10.5382/AV100.06>
- Haymon, R. M. (1983). Growth history of hydrothermal black smoker chimneys. *Nature*, 301(5902), 695–698. <https://doi.org/10.1038/301695a0>
- Herzig, P. M., Hannington, M. D., & Arribas, A., Jr. (1998). Sulfur isotopic composition of hydrothermal precipitates from the Lau back-arc: Implications for magmatic contributions to seafloor hydrothermal systems. *Mineralium Deposita*, 33(3), 226–237. <https://doi.org/10.1007/s001260050143>
- Herzig, P. M., Hannington, M. D., Scott, S. D., Maliotis, G., Rona, P. A., & Thompson, G. (1991). Gold-rich sea-floor gossans in the Troodos ophiolite and on the Mid-Atlantic Ridge. *Economic Geology*, 86(8), 1747–1755. <https://doi.org/10.2113/gsecongeo.86.8.1747>
- Hu, S., Tao, C., Liao, S., Zhu, C., & Qiu, Z. (2022). Transformation of minerals and mobility of heavy metals during oxidative weathering of seafloor massive sulfide and their environmental significance. *Science of the Total Environment*, 819, 153091. <https://doi.org/10.1016/j.scitotenv.2022.153091>
- Huang, J., Hao, J., Huang, F., & Sverjensky, D. A. (2019). Mobility of chromium in high temperature crustal and upper mantle fluids. *Geochemical Perspective Letters*, 12, 1–6. <https://doi.org/10.7185/geochemlet.1926>
- Humphris, S. E., & Thompson, G. (1978). Hydrothermal alteration of oceanic basalts by seawater. *Geochimica et Cosmochimica Acta*, 42(1), 107–125. [https://doi.org/10.1016/0016-7037\(78\)90221-1](https://doi.org/10.1016/0016-7037(78)90221-1)
- Huston, D. L., Sie, S. H., & Suter, G. F. (1995). Selenium and its importance to the study of ore genesis: The theoretical basis and its application to volcanic-hosted massive sulfide deposits using PIXE analysis. *Nuclear Instruments and Methods in Physics Research Section B: Beam Interactions with Materials and Atoms*, 104(1–4), 476–480. [https://doi.org/10.1016/0168-583X\(95\)00462-9](https://doi.org/10.1016/0168-583X(95)00462-9)
- Huston, D. L., Sie, S. H., Suter, G. F., Cooke, D. R., & Both, R. A. (1995). Trace elements in sulfide minerals from eastern Australian volcanic-hosted massive sulfide deposits; Part I, Proton microprobe analyses of pyrite, chalcopyrite, and sphalerite, and Part II, Selenium levels in pyrite; comparison with delta <sup>34</sup>S values and implications for the source of sulfur in volcanogenic hydrothermal systems. *Economic Geology*, 90(5), 1167–1196. <https://doi.org/10.2113/gsecongeo.90.5.1167>
- Jansson, N. F., & Liu, W. (2020). Controls on cobalt and nickel distribution in hydrothermal sulphide deposits in Bergslagen, Sweden—Constraints from solubility modelling. *Journal of the Geological Society of Sweden (GFF)*, 142(2), 87–95. <https://doi.org/10.1080/11035897.2020.1751270>
- Kawasumi, S., & Chiba, H. (2017). Redox state of seafloor hydrothermal fluids and its effect on sulfide mineralization. *Chemical Geology*, 451, 25–37. <https://doi.org/10.1016/j.chemgeo.2017.01.001>
- Keith, M., Haase, K. M., Klemd, R., Krumm, S., & Strauss, H. (2016). Systematic variations of trace element and sulfur isotope compositions in pyrite with stratigraphic depth in the Skouriotissa volcanic-hosted massive sulfide deposit, Troodos ophiolite, Cyprus. *Chemical Geology*, 423, 7–18. <https://doi.org/10.1016/j.chemgeo.2015.12.012>
- Keith, M., Häckel, F., Haase, K. M., Schwarz-Schampera, U., & Klemd, R. (2016). Trace element systematics of pyrite from submarine hydrothermal vents. *Ore Geology Reviews*, 72, 728–745. <https://doi.org/10.1016/j.oregeorev.2015.07.012>
- Kuznetsov, V., Maksimov, F., Zhelezov, A., Cherkashov, G., Bel'Tenev, V., & Lazareva, L. (2011). 230Th/U chronology of ore formation within the Semyenov hydrothermal district (13°31' N) at the Mid-Atlantic ridge. *Geochronometria*, 38(1), 72–76. <https://doi.org/10.2478/s13386-011-0001-1>
- Lafrance, B., Gibson, H. L., & Stewart, M. S. (2020). Chapter 4: Internal and external deformation and modification of volcanogenic massive sulfide deposits. In J. V. Rowland & D. A. Rhys (Eds.), *Applied structural geology of ore-forming hydrothermal systems, Reviews in economic geology* (Vol. 21, pp. 147–171). Littleton, Co: Society of Economic Geologists. <https://doi.org/10.5382/rev.21.04>
- Liao, S., Tao, C., Jamieson, J. W., Liu, J., Zhu, C., Barriga, F. J. A. S., et al. (2022). Oxidizing fluids associated with detachment hosted hydrothermal systems: Example from the Suye hydrothermal field on the ultraslow-spreading Southwest Indian Ridge. *Geochimica et Cosmochimica Acta*, 328, 19–36. <https://doi.org/10.1016/j.gca.2022.04.025>
- Machel, H. G., Krouse, H. R., & Sassen, R. (1995). Products and distinguishing criteria of bacterial and thermochemical sulfate reduction. *Applied Geochemistry*, 10(4), 373–389. [https://doi.org/10.1016/0883-2927\(95\)00008-8](https://doi.org/10.1016/0883-2927(95)00008-8)
- MacLeod, C. J., Searle, R. C., Murton, B. J., Casey, J. F., Mallows, C., Unsworth, S. C., et al. (2009). Life cycle of oceanic core complexes. *Earth and Planetary Science Letters*, 287(3–4), 333–344. <https://doi.org/10.1016/j.epsl.2009.08.016>
- Marques, A. F. A., Barriga, F., Chavagnac, V., & Fouquet, Y. (2006). Mineralogy, geochemistry, and Nd isotope composition of the Rainbow hydrothermal field, Mid-Atlantic Ridge. *Mineralium Deposita*, 41(1), 52–67. <https://doi.org/10.1007/s00126-005-0040-8>
- Marques, A. F. A., Barriga, F. J. A. S., & Scott, S. D. (2007). Sulfide mineralization in an ultramafic-rock hosted seafloor hydrothermal system: From serpentinization to the formation of Cu-Zn-(Co)-rich massive sulfides. *Marine Geology*, 245(1–4), 20–39. <https://doi.org/10.1016/j.margeo.2007.05.007>

- Martin, A. (2023). Fluid flow, mineralization and deformation in an oceanic detachment fault: Microtextural, geochemical and isotopic evidence from pyrite at 13°30'N on the Mid-Atlantic Ridge [Dataset]. Mendeley Data, V1. <https://doi.org/10.17632/pp3ymvhvcp.1>
- Martin, A. J., Jamieson, J. W., de Ronde, C. E. J., Humphris, S. E., McDonald, I., Layne, G. D., et al. (2022b). Trace metal and sulfur cycling in a hydrothermally active arc volcano: Deep-sea drilling of the brothers volcano, Kermadec arc, New Zealand. *Mineralium Deposita*, 58(2), 403–425. <https://doi.org/10.1007/s00126-022-01135-x>
- Martin, A. J., Jamieson, J. W., de Ronde, C. E. J., Humphris, S. E., Roberts, S., MacLeod, C. J., et al. (2022a). Hydrothermal alteration within the brothers submarine arc volcano, Kermadec arc, New Zealand. *Economic Geology*, 118(7), 1657–1679. <https://doi.org/10.5382/econgeo.4962>
- Martin, A. J., Jamieson, J. W., de Ronde, C. E. J., Layne, G. D., Piercey, G., & Brandl, P. A. (2023). Constraining temporal variations in metal and sulfur sources using high-resolution mineral-scale analysis of pyrite: Evidence from the Brothers volcano, Kermadec arc, New Zealand. *Mineralium Deposita*, 58(7), 1237–1262. <https://doi.org/10.1007/s00126-023-01177-9>
- Martin, A. J., Keith, M., Parvaz, D. B., McDonald, I., Boyce, A. J., McFall, K. A., et al. (2019). Effects of magmatic volatile influx in mafic VMS hydrothermal systems: Evidence from the Troodos ophiolite, Cyprus. *Chemical Geology*, 531, 119325. <https://doi.org/10.1016/j.chemgeo.2019.119325>
- Martin, A. J., McDonald, I., Jamieson, J. W., Jenkin, G. R. T., McFall, K. A., Piercey, G., et al. (2021). Mineral-scale variation in the trace metal and sulfur isotope composition of pyrite: Implications for metal and sulfur sources in mafic VMS deposits. *Mineralium Deposita*, 57(6), 911–933. <https://doi.org/10.1007/s00126-021-01080-1>
- Martin, A. J., McDonald, I., MacLeod, C. J., Prichard, H. M., & McFall, K. (2018). Extreme enrichment of selenium in the Apliki Cyprus-type VMS deposit, Troodos, Cyprus. *Mineralogical Magazine*, 82(3), 697–724. <https://doi.org/10.1180/mgm.2018.81>
- Maslennikov, V. V., Maslennikova, S. P., Large, R. R., & Danyushevsky, L. V. (2009). Study of trace element zonation in vent chimneys from the Silurian Yaman-Kasy volcanic-hosted massive sulfide deposit (southern Urals, Russia) using laser ablation-inductively coupled plasma mass spectrometry (LA-ICPMS). *Economic Geology*, 104(8), 1111–1141. <https://doi.org/10.2113/econgeo.104.8.1111>
- Melekestseva, I., Maslennikov, V., Tret'yakov, G., Maslennikova, S., Danyushevsky, L., Kotlyarov, V., et al. (2020). Trace Element Geochemistry of Sulfides from the Ashadze-2 Hydrothermal Field (12°58'N, Mid-Atlantic Ridge): Influence of Host Rocks, Formation Conditions or Seawater? *Minerals*, 10(9), 743. <https://doi.org/10.3390/min10090743>
- Melekestseva, I., Maslennikov, V. V., Safina, N. P., Nimis, P., Maslennikova, S., Beltenev, V., et al. (2018). Sulfide Breccias from the Semenov-3 Hydrothermal Field, Mid-Atlantic Ridge: Authigenic Mineral Formation and Trace Element Pattern. *Minerals*, 8(8), 321. Article 8. <https://doi.org/10.3390/min8080321>
- Melekestseva, I. Y., Maslennikov, V. V., Tret'yakov, G. A., Nimis, P., Beltenev, V. E., Rozhdestvenskaya, I., et al. (2017). Gold- and Silver-Rich Massive Sulfides from the Semenov-2 Hydrothermal Field, 13°31.13'N, Mid-Atlantic Ridge: A Case of Magmatic Contribution? *Economic Geology*, 112(4), 741–773. <https://doi.org/10.2113/econgeo.112.4.741>
- Melekestseva, I. Y., Tret'yakov, G. A., Nimis, P., Yuminov, A. M., Maslennikov, V. V., Maslennikova, S. P., et al. (2014). Barite-rich massive sulfides from the Semenov-1 hydrothermal field (Mid-Atlantic Ridge, 13°30.87'N): Evidence for phase separation and magmatic input. *Marine Geology*, 349, 37–54. <https://doi.org/10.1016/j.margeo.2013.12.013>
- Murton, B. J., Lehrmann, B., Dutrieux, A. M., Martins, S., de la Iglesia, A. G., Stobbs, I. J., et al. (2019). Geological fate of seafloor massive sulphides at the TAG hydrothermal field (Mid-Atlantic Ridge). *Ore Geology Reviews*, 107, 903–925. <https://doi.org/10.1016/j.oregeorev.2019.03.005>
- Ohmoto, H. (2003). Nonredox transformations of magnetite-hematite in hydrothermal systems. *Economic Geology*, 98(1), 157–161. <https://doi.org/10.2113/econgeo.98.1.157>
- Peirce, C., Robinson, A. H., Funnell, M. J., Searle, R. C., MacLeod, C. J., & Reston, T. J. (2020). Magmatism versus serpentinization—Crustal structure along the 13°N segment at the Mid-Atlantic Ridge. *Geophysical Journal International*, 221(2), 981–1001. <https://doi.org/10.1093/gji/ggaa052>
- Pertsev, A. N., Bortnikov, N. S., Vlasov, E. A., Beltenev, V. E., Dobretsova, I. G., & Ageeva, O. A. (2012). Recent massive sulfide deposits of the Semenov ore district, Mid-Atlantic Ridge, 13°31'N: Associated rocks of the oceanic core complex and their hydrothermal alteration. *Geology of Ore Deposits*, 54(5), 334–346. <https://doi.org/10.1134/S1075701512050030>
- Petersen, S., Herzig, P. M., & Hannington, M. D. (2000). Third dimension of a presently forming VMS deposit: TAG hydrothermal mound, Mid-Atlantic Ridge, 26°N. *Mineralium Deposita*, 35(2–3), 233–259. <https://doi.org/10.1007/s001260050018>
- Petersen, S., Herzig, P. M., Hannington, M. D., Jonasson, I. R., & Arribas, A., Jr. (2002). Submarine gold mineralization near Lihir Island, New Ireland Fore-Arc, Papua New Guinea. *Economic Geology*, 97(8), 1795–1813. <https://doi.org/10.2113/econgeo.97.8.1795>
- Rees, C. E., Jenkins, W. J., & Monster, J. (1978). The sulphur isotopic composition of ocean water sulphate. *Geochimica et Cosmochimica Acta*, 42(4), 377–381. [https://doi.org/10.1016/0016-7037\(78\)90268-5](https://doi.org/10.1016/0016-7037(78)90268-5)
- Reich, M., Deditius, A., Chrysosoulis, S., Li, J.-W., Ma, C.-Q., Parada, M. A., et al. (2013). Pyrite as a record of hydrothermal fluid evolution in a porphyry copper system: A SIMS/EMP trace element study. *Geochimica et Cosmochimica Acta*, 104, 42–62. <https://doi.org/10.1016/j.gca.2012.11.006>
- Revan, M. K., Genç, Y., Maslennikov, V. V., Maslennikova, S. P., Large, R. R., & Danyushevsky, L. V. (2014). Mineralogy and trace-element geochemistry of sulfide minerals in hydrothermal chimneys from the Upper-Cretaceous VMS deposits of the eastern Pontide orogenic belt (NE Turkey). *Ore Geology Reviews*, 63, 129–149. <https://doi.org/10.1016/j.oregeorev.2014.05.006>
- Reyes, A. G. (1990). Petrology of Philippine geothermal systems and the application of alteration mineralogy to their assessment. *Journal of Volcanology and Geothermal Research*, 43(1–4), 279–309. [https://doi.org/10.1016/0377-0273\(90\)90057-M](https://doi.org/10.1016/0377-0273(90)90057-M)
- Ruiz-Agudo, E., Putnis, C. V., & Putnis, A. (2014). Coupled dissolution and precipitation at mineral–fluid interfaces. *Chemical Geology*, 383, 132–146. <https://doi.org/10.1016/j.chemgeo.2014.06.007>
- Sakai, H., Marais, D. J. D., Ueda, A., & Moore, J. G. (1984). Concentrations and isotope ratios of carbon, nitrogen and sulfur in ocean-floor basalts. *Geochimica et Cosmochimica Acta*, 48(12), 2433–2441. [https://doi.org/10.1016/0016-7037\(84\)90295-3](https://doi.org/10.1016/0016-7037(84)90295-3)
- Schiffman, P., & Fridleifsson, G. O. (1991). The smectite–chlorite transition in drillhole NJ-15, Nesjavellir geothermal field, Iceland: XRD, BSE and electron microprobe investigations. *Journal of Metamorphic Geology*, 9(6), 679–696. <https://doi.org/10.1111/j.1525-1314.1991.tb00558.x>
- Seyfried, W. E., Jr., Ding, K., Berndt, M. E., & Chen, X. (1999). Experimental and theoretical controls on the composition of mid-ocean ridge hydrothermal fluids. In C. T. Barrie & M. D. Hannington (Eds.), *Volcanic-associated massive sulfide deposits; processes and examples in modern and ancient settings, Reviews in economic geology* (Vol. 8, pp. 181–200). Society of Economic Geologists. <https://doi.org/10.5382/Rev.08.08>
- Smith, D. K., Escartin, J., Schouten, H., & Cann, J. R. (2008). Fault rotation and core complex formation: Significant processes in seafloor formation at slow-spreading mid-ocean ridges (Mid-Atlantic Ridge, 13°–15°N). *Geochemistry, Geophysics, Geosystems*, 9(3), Q03003. <https://doi.org/10.1029/2007GC001699>

- Steadman, J. A., Large, R. R., Olin, P. H., Danyushevsky, L. V., Meffre, S., Huston, D., et al. (2021). Pyrite trace element behavior in magmatic-hydrothermal environments: An LA-ICPMS imaging study. *Ore Geology Reviews*, *128*, 103878. <https://doi.org/10.1016/j.oregeorev.2020.103878>
- Tanner, D., Henley, R. W., Mavrogenes, J. A., & Holden, P. (2013). Combining in situ isotopic, trace element and textural analyses of quartz from four magmatic-hydrothermal ore deposits. *Contributions to Mineralogy and Petrology*, *166*(4), 1119–1142. <https://doi.org/10.1007/s00410-013-0912-3>
- Tanner, D., Henley, R. W., Mavrogenes, J. A., & Holden, P. (2016). Sulfur isotope and trace element systematics of zoned pyrite crystals from the El Indio Au–Cu–Ag deposit, Chile. *Contributions to Mineralogy and Petrology*, *171*(4), 33. <https://doi.org/10.1007/s00410-016-1248-6>
- Verlaguet, A., Bonnemains, D., Mével, C., Escartin, J., Andreani, M., Bourdelle, F., et al. (2021). Fluid circulation along an oceanic detachment fault: Insights from fluid inclusions in silicified brecciated fault rocks (Mid-Atlantic Ridge at 13°20'N). *Geochemistry, Geophysics, Geosystems*, *22*(1), e2020GC009235. <https://doi.org/10.1029/2020GC009235>
- Von Damm, K. L. (1990). Seafloor hydrothermal activity: Black smoker chemistry and chimneys. *Annual Review of Earth and Planetary Sciences*, *18*(1), 173–204. <https://doi.org/10.1146/annurev.ea.18.050190.001133>
- Watson, E. B., Cherniak, D. J., & Frank, E. A. (2009). Retention of biosignatures and mass-independent fractionations in pyrite: Self-diffusion of sulfur. *Geochimica et Cosmochimica Acta*, *73*(16), 4792–4802. <https://doi.org/10.1016/j.gca.2009.05.060>
- Yıldırım, N., Dönmez, C., Kang, J., Lee, I., Pirajno, F., Yıldırım, E., et al. (2016). A magnetite-rich Cyprus-type VMS deposit in Ortaklar: A unique VMS style in the Tethyan metallogenic belt, Gaziantep, Turkey. *Ore Geology Reviews*, *79*, 425–442. <https://doi.org/10.1016/j.oregeorev.2016.05.021>
- Zeng, Z., Ma, Y., Chen, S., Selby, D., Wang, X., & Yin, X. (2017). Sulfur and lead isotopic compositions of massive sulfides from deep-sea hydrothermal systems: Implications for ore genesis and fluid circulation. *Ore Geology Reviews*, *87*, 155–171. <https://doi.org/10.1016/j.oregeorev.2016.10.014>
- Zhao, J., Brugger, J., & Pring, A. (2019). Mechanism and kinetics of hydrothermal replacement of magnetite by hematite. *Geoscience Frontiers*, *10*(1), 29–41. <https://doi.org/10.1016/j.gsf.2018.05.015>